Fermi National Accelerator Laboratory

Diffractive Production of ρ^0 (770) Mesons in Muon-Proton Interactions at 470 GeV

M.R. Adams et al.

The E665 Collaboration

Fermi National Accelerator Laboratory
P.O. Box 500, Batavia, Illinois 60510

April 1997

Disclaimer

Distribution

Diffractive production of $\rho^0(770)$ mesons in muon-proton interactions at 470 GeV

E665 Collaboration

M.R. Adams[6], M. Aderholz[12], S. Aïd[10,a], P.L. Anthony[9,b], D.A. Averill[6], M.D. Baker[11], B.R. Baller[4], A. Banerjee[15,c], A.A. Bhatti[16,d], U. Bratzler[16,e], H.M. Braun[17], T.J. Carroll[12,f], H.L. Clark[14,g], J.M. Conrad[5,h], R. Davisson[16], I. Derado[12], F.S. Dietrich[9], W. Dougherty[16], T. Dreyer[1], V. Eckardt[12], U. Ecker[17,i], M. Erdmann[1,j], G.Y. Fang[5,k], J. Figiel[8], R.W. Finlay[14], H.J. Gebauer[12], D.F. Geesaman[2], K.A. Griffioen[15,l], R.S. Guo[6,m], J. Haas[1], C. Halliwell[6], D. Hantke[12,n], K.H. Hicks[14], H.E. Jackson[2], D.E. Jaffe[6,o], G. Jancso[7], D.M. Jansen[16,p], Z. Jin[16], K. Kadija[12], S. Kaufmann[2], R.D. Kennedy[3,q], E.R. Kinney[2,r], H.G.E. Kobrak[3], A.V. Kotwal[5,h], S. Kunori[10], J.J. Lord[16], H.J. Lubatti[16], D. McLeod[6], P. Madden[3,s], S. Magill[6,t], A. Manz[12], H. Melanson[4], D.G. Michael[5,u], H.E. Montgomery[4], J.G. Morfin[4], R.B. Nickerson[5,v], J. Novak[13,w], K. Olkiewicz[8], L. Osborne[11], R. Otten[17], V. Papavassiliou[2,x], B. Pawlik[8], F.M. Pipkin[5,*], D.H. Potterveld[2], A. Röser[17,y], J.J. Ryan[11,z], C.W. Salgado[4,aa], H. Schellman[13], M. Schmitt[5,bb], N. Schmitz[12], K.P. Schüler[18,z], G. Siegert[1,cc], A. Skuja[10], G.A. Snow[10], S. Söldner-Rembold[12,dd], P. Spentzouris[13,h], P. Stopa[8], R.A. Swanson[3], H. Venkataramania[13], M. Wilhelm[1,ee], Richard Wilson[5], W. Wittek[12], S.A. Wolbers[4], G.P. Zeller[13], A. Zghiche[2], and T. Zhao[16]

1   Albert-Ludwigs-Universität Freiburg i. Br., Germany
2   Argonne National Laboratory , Argonne, Illinois 60439
3   University of California, San Diego, California 92093
4   Fermi National Accelerator Laboratory, Batavia, Illinois 60510
5   Harvard University, Cambridge, Massachusetts 02138
6   University of Illinois, Chicago, Illinois 60680
7   KFKI Research Institute for Particle and Nuclear Physics, H-1525 Budapest, Hungary
8   Institute for Nuclear Physics, Krakow, Poland
9   Lawrence Livermore National Laboratory, Livermore, California 94551
10   University of Maryland, College Park, Maryland 20742
11   Massachusetts Institute of Technology, Cambridge, Massachusetts 02139
12   Max-Planck-Institut für Physik, Munich, Germany
13   Northwestern University, Evanston, Illinois 60208
14   Ohio University, Athens, Ohio 45701
15   University of Pennsylvania, Philadelphia, Pennsylvania 19104
16   University of Washington, Seattle, Washington 98195
17   University of Wuppertal, Wuppertal, Germany
18   Yale University, New Haven, Connecticut 06511

Present addresses:

* deceased

a University of Hamburg, D-22603 Hamburg, Germany.

b SLAC, Stanford, CA 94309, USA.

c Fidelity Investments Corp., Boston, MA, USA.

d The Rockefeller University, New York NY 10021, USA.

e Max-Planck-Institut für Physik, D-80805 München, Germany.

f University of Wisconsin Hospital, Madison, WI 53792, USA.

g Texas A&M University, College Station, TX 77843, USA.

h Columbia University, New York, NY 10027, USA.

i Jenfelderstr. 147, D-22045 Hamburg, Germany.

j Heidelberg University, D-69120, Heidelberg Germany.

k Dept. of Medical Physics, University of Wisconsin, Madison, WI 53706, USA.

l College of William and Mary, Williamsburg, VA 23187, USA.

m Department of Physics, National Kaohsiung Normal University, Kaohsiung, Taiwan.

n GSF - Forschungszentrum für Umwelt und Gesundheit GmbH, D-85764 Oberschleißheim, Germany.

o SCRI, Florida State University, Tallahassee, FL 32606, USA.

p LANL, Los Alamos, NM 87545, USA.

q Fermi National Accelerator Laboratory, Batavia, IL 60510, USA.

r University of Colorado, Boulder, CO 80309, USA.

s Linear Technology Inc., Milpitas, CA 95395, USA.

t Argonne National Laboratory, Argonne, IL 60439, USA.

u California Institute of Technology, Pasadena, CA 91125, USA.

v Oxford University, Oxford OX1 3RH, UK.

w Yale University, New Haven, CT 06511, USA.

x New Mexico State University, Las Cruces, NM 88003, USA.

y Klinikum Barmen, Abt. Radiologie, D-42283 Wuppertal, Germany.

z DESY, D-22603 Hamburg, Germany.

aa Thomas Jefferson National Accelerator Facility, Newport News, VA 23606, USA.

bb CERN, CH-1211 Geneva 23, Switzerland.

cc University of Wuppertal, D-42119 Wuppertal, Germany.

dd Albert-Ludwigs-Universität Freiburg, D-79104 Freiburg, Germany.

ee Hoffmann-LaRoche, CH-4002 Basel, Switzerland.

Abstract. The diffractive production of $\rho^0(770)$ mesons in muon-proton interactions is studied in the kinematic region $0.15\ \mathrm{GeV}^2 < Q^2 < 20\ \mathrm{GeV}^2$ and $20\ \mathrm{GeV} < \nu < 420\ \mathrm{GeV}$. The data were obtained in the Fermilab fixed-target experiment E665 with primary muons of 470 GeV energy. Results are presented on the Q^2, x and ν dependence of the cross section, on the shape of the $\pi^+\pi^-$ mass spectrum, on the slope of the diffraction peak and on the production and decay angular distributions of the $\rho^0(770)$. The cross section for diffractive production of ρ^0 by virtual photons on protons depends mainly on Q^2. At fixed Q^2, no significant dependence on x or ν is observed. The extrapolation to $Q^2 = 0$ yields a photoproduction cross section of $(10.30 \pm 0.33)\ \mu\mathrm{b}$. The slope of the t' distribution has a value of $(7.0\pm0.2)\ \mathrm{GeV}^{-2}$, with a tendency to decrease as Q^2 increases. The production and decay angular distributions of the ρ^0 depend strongly on Q^2 and are consistent with s-channel helicity conservation. The ratio $R = \sigma_L/\sigma_T$ deduced from the decay angular distributions rises strongly with Q^2, passing the value of 1 at $Q^2 \approx 2\ \mathrm{GeV}^2$.

1 Introduction

For many years diffractive production of the $\rho^0(770)$ has been the subject of photoproduction [1, 2, 3, 4, 5, 6, 7, 8, 9], electroproduction [10, 11, 12, 13, 14, 15, 16, 17, 18, 19] and muoproduction [20, 21, 22, 23, 24, 25, 26, 27] experiments. Theoretical investigations are based on the vector-dominance-model [28], on perturbative QCD [29, 30, 31, 32, 33, 34] and on models of the pomeron [35, 36, 37, 38, 39, 40].

The present paper of the E665 Collaboration presents measurements of diffractive production of $\rho^0(770)$ mesons by muons on protons in the kinematic region 20 GeV $< \nu < 420$ GeV and $0.15\ \mathrm{GeV}^2 < Q^2 < 20\ \mathrm{GeV}^2$. The experiment extends the EMC/NMC [23, 24, 25, 26, 27] measurements to higher ν and lower Q^2 values. E665 covers a similar region in Q^2 to the CHIO [22] experiment, however with higher statistics and with a larger range in ν.

The paper is organized as follows. Section 2 gives a general description of the experiment. Section 3 deals with the Monte Carlo simulation, which is essential for the corrections to be applied. The experimental procedure for producing the final corrected results from the raw data is explained in Section 4. The results are compiled in Section 5, and a summary is given in Section 6.

2 The Experiment

This analysis uses data obtained in the 1991 run of the Fermilab fixed target experiment E665. Details of the E665 spectrometer have been documented elsewhere [41]; only those components which are germane to this analysis will be discussed.
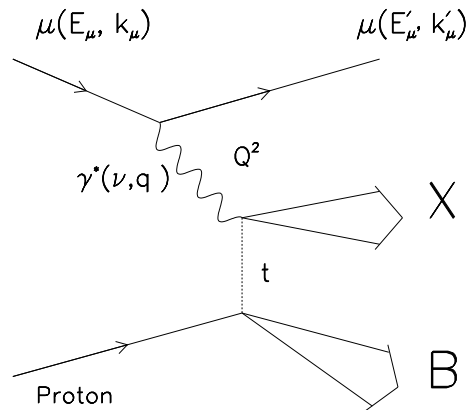

Fig. 1. Diffractive production of a mesonic system X and a baryonic system B in the reaction $\mu p \rightarrow \mu X B$.

2.1 Definition of Variables

At the energies of the present experiment, one-photon exchange is the dominant process in the muon-proton interaction: an incident muon of energy E_μ scatters through an angle θ_μ by exchanging a virtual photon with the target proton of mass M_p. This interaction is described in terms of the following variables: the leptonic energy transfer ν in the laboratory system, the virtuality of the exchanged photon Q^2 and $x = Q^2/2M_p\nu$. The hadronic center of mass system (cms) is the rest frame of the system formed by the virtual photon and the target proton. The forward region in the cms is the hemisphere for which the virtual-photon direction defines the pole.

Figure 1 shows a diagram of diffractive production of a mesonic system X and a baryonic system B in the reaction $\mu p \rightarrow \mu X B$. In this paper only results for the specific case where X is the $\rho^0(770)$ meson will be presented. The process in which only the virtual photon dissociates, while the proton stays intact, is called single-diffraction dissociation (SD). In this case the mass M_B of the baryonic system is equal to the proton mass. If in addition the proton dissociates into a system B with a mass $M_B > M_p$, the process is called double-diffraction dissociation (DD). The terms single diffraction and double diffraction dissociation were introduced in studies of diffractive production in hadronic interactions [42]. The negative square of the four-momentum transferred from the virtual photon to the proton is denoted by t. The minimum value $t_{\min}$ of t for fixed ν, Q^2, M_X and M_B corresponds to the limit of collinear three-momenta of the virtual photon and the system X in the laboratory system. Diffractive processes are characterized by small values of t, typically less than $1\ \mathrm{GeV}^2$.

A full summary of the kinematic variables appears in Table 1.

2.2 Beam

The momentum distribution of the E665 muon beam had a mean of 470 GeV/c and a root mean square deviation

of 56 GeV/c. Incident muons passed through the E665 beam spectrometer before impinging on the target. The beam spectrometer determined the energy and trajectory of the muon, formed fast Level I trigger signals, and determined the integrated beam flux for normalization [43]. The momentum resolution of the beam spectrometer, $\delta p/p$, was typically 0.4%.

2.3 Target

In the 1991 run of E665, liquid targets of hydrogen and deuterium were interchanged approximately once per Tevatron cycle (58 seconds). This analysis is concerned only with the hydrogen target. The hydrogen density was 0.0704 g/cm³. The length of the hydrogen target was 99.1 cm, corresponding to 0.1374 (0.1140) of a nuclear interaction (radiation) length.

2.4 Forward Spectrometer

An open geometry spectrometer, instrumented with multiwire proportional chambers and drift chambers, determined the scattering angle and energy of the scattered muon upstream of 3 meters of steel, which served as a hadron absorber. The forward spectrometer provided a momentum resolution, $\delta p/p$, of better than 1.5% and an angular resolution of 40 μrad, for the scattered muon. Muons were identified by matching tracks reconstructed in the forward spectrometer with tracks found in four stations of proportional tubes and scintillating hodoscope planes located downstream of the hadron absorber. In addition, a gas sampling electromagnetic calorimeter was located in front of the hadron absorber. It had a resolution of $\delta E/E = (0.38)/\sqrt{E/\text{GeV}}$ [43] for photons and electrons with energies below 80 GeV. The calorimeter was used to identify and remove background events, primarily elastic muon-electron (μe) scatters, and radiative events in which a large fraction of the available energy is taken by a bremsstrahlung photon.

2.5 Trigger

In the present analysis only data obtained with the small-angle trigger (SAT) were included: each beam trajectory, defined by the beam spectrometer hodoscope elements, was projected to the scintillation hodoscopes located downstream of the hadron absorber. In order to fulfill the SAT condition the absence of a signal in a veto region around the projected beam trajectory was required. The SAT made it possible to trigger at scattering angles as small as 1 milliradian corresponding to Q^2 of ≈ 0.15 GeV². A relevant feature of the SAT was the use of a veto counter located upstream of the hadron absorber, in addition to the veto counters located behind the absorber. The upstream veto element reduced the rate of spurious triggers from muon scatters in the absorber.

3 Monte-Carlo simulation

For the analysis of diffractive production in the present experiment a special Monte Carlo program for muon-nucleon and muon-nucleus scattering has been developed. The program generates non-diffractive and diffractive events. For nuclear targets (not used in this paper), coherent diffractive events are generated in addition and the nuclear shadowing of the inelastic cross section and of the coherent and incoherent diffractive cross section are simulated. Radiative effects are taken into account by the GAMRAD program [44], which is based on the formulae in [45, 46]. The particles produced at the interaction vertex are tracked through the E665 detector, simulating decays, photon conversions, reinteractions, multiple scattering and energy loss in the detector material [47]. Finally, the detector response to the passage of all produced particles and the triggers are simulated taking into account the chamber efficiencies and resolutions. The Monte Carlo generated events were subjected to the same reconstruction and analysis as the data.

The sequence of operations for the generation of the primary interactions on the nucleon is as follows:

- Generation of the energy E_μ of the incident muon according to the experimental beam energy spectrum.
- Generation of (x, Q^2) according to the inelastic cross section $d\sigma_{inel}/dx\,dQ^2(E_\mu, x, Q^2)$ for $\mu p \to \mu H$, where H stands for any hadronic system. For the calculation of $d\sigma_{inel}/dx\,dQ^2$ a set of parton distributions by Donnachie and Landshoff [48] and $R = \sigma_L/\sigma_T$ from [49] are used.
- Decision to generate a diffractive or non-diffractive event according to the probability P for a diffractive $\left(P_{diff} = \frac{d\sigma_{diff}(E_\mu, \nu, Q^2)}{d\nu\,dQ^2} \middle/ \frac{d\sigma_{inel}(E_\mu, \nu, Q^2)}{d\nu\,dQ^2} \right)$ or non-diffractive $(P_{non-diff} = 1 - P_{diff})$ interaction. Here σ_{diff} is the cross section for diffractive interactions, including single-diffraction dissociation (SD, i.e. diffractive dissociation of the virtual photon) and double-diffraction dissociation (DD, i.e. additional dissociation of the target nucleon). σ_{diff} is calculated by the generator GENDIF (see below).
- Generation of hadrons: In the case of a non-diffractive event, hadrons are generated by calling a standard Lund generator (LEPTO 5.2 [50], JETSET 6.3 [51]); in the case of a diffractive event, by calling the E665 generator GENDIF.

GENDIF simulates the production of the following mesonic diffractive systems: $\rho^0(770)$, $\omega(783)$, $\phi(1020)$, $\rho'_1(1450)$, $\rho'_2(1700)$ and a continuum of diffractive masses M_X greater than 2 GeV.

The main operations in GENDIF are the following: The cross section for diffractive ρ^0 production, $\mu p \to \mu\rho^0 p$, is calculated as [70, 52, 28]

$$\frac{d\sigma}{d\nu\,dQ^2}(E_\mu, \nu, Q^2) = \Gamma_T \cdot (1 + \epsilon R) \cdot P_\rho^2 \cdot \sigma(\gamma p \to \rho^0 p) \,. \quad (1)$$

Γ_T is the flux of transversely polarized virtual photons

$$\Gamma_T = \frac{\alpha(\nu - Q^2/2M_p)}{2\pi Q^2 E_\mu^2 (1 - \epsilon)}, \tag{2}$$

α is the fine-structure constant, ϵ is the ratio of the fluxes for longitudinally and transversely polarized virtual photons

$$\epsilon = \frac{\Gamma_L}{\Gamma_T} = \frac{1 - (\nu/E_\mu) - (Q^2/4E_\mu^2)}{1 - (\nu/E_\mu) + \frac{1}{2}(\nu/E_\mu)^2 + (Q^2/4E_\mu^2)}. \tag{3}$$

$R = \sigma_L/\sigma_T$ is the ratio of cross sections for ρ^0 production by longitudinally and transversely polarized virtual photons. P_ρ is the ρ^0 propagator

$$P_\rho = \frac{M_\rho^2}{Q^2 + M_\rho^2}, \tag{4}$$

with M_ρ being the central mass value of the ρ^0, and $\sigma(\gamma p \to \rho^0 p)$ is the photoproduction cross section at a photon beam energy equal to ν, not to be confused with $\sigma_{diff}(\gamma^* p \to \rho^0 p)$ of eq. (23) which is a function of ν and Q^2.

The cross sections for the vector mesons (V) ω, ϕ, ρ_1', and ρ_2' are determined on the basis of photoproduction cross section measurements and assuming

$$\frac{d\sigma/d\nu dQ^2 (\mu p \to \mu V p)}{d\sigma/d\nu dQ^2 (\mu p \to \mu \rho^0 p)} = \frac{P_V^2}{P_\rho^2} \frac{\sigma(\gamma p \to V p)}{\sigma(\gamma p \to \rho^0 p)}. \tag{5}$$

The cross section for the continuum is taken from [53]

$$\frac{d\sigma_{diff}(\mu p \to \mu p X)}{d\nu dQ^2 dM_X^2} = \frac{d\sigma_{inel}(\mu p \to \mu H)}{d\nu dQ^2} \tag{6}$$

$$\cdot \left\{ 2r_D \frac{Q^2 M_X^2}{(Q^2 + M_X^2)^3} + \frac{A_{3P}}{b_{3P}} \frac{M_X^4}{(Q^2 + M_X^2)^3} \right\}$$

with $r_D = 0.1$, $A_{3P} = 0.16$ GeV^{-2} and $b_{3P} = 5.5$ GeV^{-2}.

The cross sections for the vector mesons and the continuum are increased by a factor $1/(1 - 0.20)$ to include the contribution from double-diffraction dissociation, which is assumed to be $h = DD/(SD + DD) = 20\%$ of the total diffractive cross section, independent of M_X. Based on measurements in hadron-hadron collisions, h for diffractive ρ^0 production in leptoproduction has been estimated as $h = 0.21$ to 0.23 [54]. A recent measurement by the H1 experiment [55] yields $DD/SD = 0.59 \pm 0.12 \pm 0.12$ for diffractive ρ^0 production, corresponding to $h = 0.37 \pm 0.05 \pm 0.05$. The effect on the cross section results due to the value of h assumed in the Monte Carlo generation is discussed in Sect. 4.5.

The various vector mesons and the continuum are generated according to these cross sections. The mass distributions for the vector mesons are given by Breit-Wigner functions. The mass distribution for the continuum is given by (6).

The mass spectrum of the baryonic system resulting from the dissociation of the target nucleon in the double-diffraction dissociation events is calculated as

$$M_B^2 \frac{d\sigma}{dM_B^2} = \tag{7}$$

$$\begin{cases} C \cdot \dfrac{M_B^2 - (M_p + M_\pi)^2}{1.8 \text{ GeV}^2 - (M_p + M_\pi)^2} & \text{for } M_B^2 \leq 1.8 \text{ GeV}^2 \\ C & \text{for } M_B^2 \geq 1.8 \text{ GeV}^2 \end{cases}$$

in which C is a constant and M_π is the pion mass. This parametrization is suggested by measurements of pp diffractive scattering [56].

The t values are generated assuming an exponential dependence $d\sigma/dt \propto e^{-bt}$. For single-diffraction dissociation events b is taken to be 6.5 GeV^{-2} for the ρ^0 and ω, 6.0 GeV^{-2} for the ϕ and 5.0 GeV^{-2} for the remaining contributions. For double diffraction dissociation events the same b values are used if M_B is less than 2 GeV, whereas the values are divided by 2 if M_B is greater than 2 GeV [56].

The decay pions of the ρ^0 are generated according to unpublished preliminary values of the decay density matrix element r_{00}^{04} as measured by this experiment. The ω and ϕ decays are simulated assuming unpolarized states and using standard Lund routines [51].

The multiple charged and neutral hadron branching ratios for ρ_1' and ρ_2' decays were assigned according to rough experimental observations [57]. The decays are simulated according to the longitudinal phase space algorithm [58, 59, 60].

The decay of the continuum at a fixed mass M_X is assumed to be described by the hadronic final state in $e^+ e^-$ interactions at $\sqrt{s} = M_X$. The latter is simulated using standard Lund routines. The direction defined by the q and $\overline{q}$ in the $e^+ e^-$ interaction is aligned with the direction of the virtual photon in the rest frame of the diffractive system, and is then smeared according to the prescription described in [61].

In DD events, the multiplicity distributions for charged and neutral hadrons from the decay of the baryonic system B are assumed to be Gaussian [62, 42]

$$P(n) \sim \frac{1}{D} \exp\left(-\frac{(n - n_0)^2}{2D^2} \right) \tag{8}$$

$$n = \begin{cases} n_{ch} = 1, 3, \ldots & \text{(multiplicity of charged hadrons)} \\ n_{neu} = 0, 1, 2, \ldots & \text{(multiplicity of neutral hadrons)} \end{cases}$$

with

$$n_0 = \begin{cases} 2\sqrt{(M_B - M_p)/\text{GeV}} & \text{for charged hadrons} \\ \sqrt{(M_B - M_p)/\text{GeV}} & \text{for neutral hadrons} \end{cases}$$

$$D = n_0/2$$

and $\quad n_{ch} + n_{neu} \geq 2$. \tag{9}

The momenta of the decay hadrons are generated according to longitudinal phase space.

The initially generated quantities for the primary μp interactions are called the "MC true" quantities, the corresponding sample of events is denoted by "MC true" sample. The quantities after simulating the detector and after reconstruction of the events are called the "MC reconstructed" quantities. The corresponding event sample is the "MC reconstructed" sample.
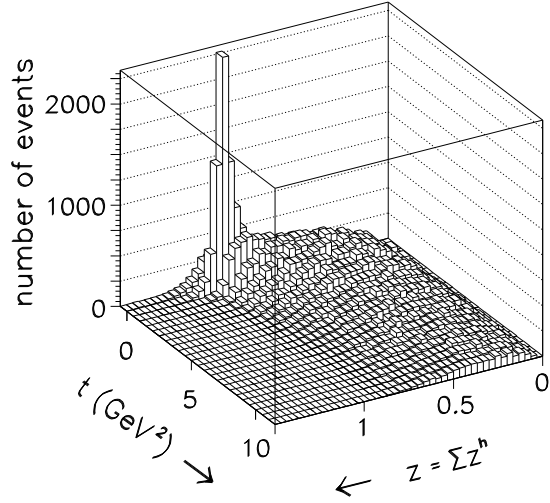
Fig. 2. Distribution of events in the (t, z) plane for the inelastic sample. The accumulation of events at (low t, high z) is a clear signal for diffractive production.

4 Experimental procedure

4.1 Selection of data and definition of "inelastic sample"

In order to be accepted in the analysis a reconstructed event has to fulfill the following criteria:

the small-angle trigger (SAT) has fired

$$320 \text{ GeV} < E_\mu < 650 \text{ GeV}$$
$$\theta_\mu > 0.001 \text{ rad}$$
$$Q^2 > 0.15 \text{ GeV}^2$$
$$20 \text{ GeV} < \nu < 420 \text{ GeV} \tag{10}$$
$$0.0001 < x < 0.6$$
$$0.05 < y < 0.8$$

$$\frac{\Delta Q^2}{Q^2} < 0.20$$
$$\frac{\Delta \nu}{\nu} < 0.20 \tag{11}$$
$$\text{number of accepted hadrons} \geq 2$$
$$E_{big} < 0.35 \, \nu \, .$$

ΔQ^2 and $\Delta \nu$ are the measurement errors of Q^2 and ν, respectively. E_{big} is the highest-energy cluster in the electromagnetic calorimeter. An "accepted" hadron is a charged hadron with a relative momentum error less than 30%, which according to the geometrical vertex fit is produced at the interaction vertex defined by the trajectories of the incident and scattered muon.

The cuts on E_μ, x, Q^2 and θ_μ are essentially given by the beam and trigger conditions. The lower cuts in ν and y exclude the region of low resolution in ν, the upper cut in y is chosen in order to reduce the contribution from radiative events. A true event is called "radiative"

if a real bremsstrahlung photon with momentum greater than 300 MeV is emitted.

These selections are not sufficient to suppress to an acceptable level the background from elastic muon-electron (μe) scatters in the region $x < 5.5 \cdot 10^{-4}$ and $Q^2 < 0.5 \text{ GeV}^2$. The additional requirement on the number of accepted hadrons removes the μe events nearly completely. It also reduces the contribution from radiative events. Radiative events are further suppressed by the selection in E_{big}. From Monte Carlo calculations the fraction of events removed by this latter cut is estimated to be 3.2% for the sample of "non-radiative" events and 12.7% for the sample of "radiative" events.

The sample of reconstructed events defined by these selections is called the "inelastic sample". It consists of 143 502 events. The corresponding sample of reconstructed Monte Carlo events contains 221 210 events. For the experimental data, the average values of E_μ, ν, Q^2, x and W are 458 GeV, 153 GeV, 2.5 GeV^2, 0.013 and 16.1 GeV, those of $\log(Q^2/\text{GeV}^2)$ and $\log x$ are 0.009 and -2.4, respectively. Throughout this paper "log" denotes the logarithm to the base 10.

Reconstructed charged hadrons are assumed to be pions, except for the following case: if the system of accepted hadrons consists of a positive and a negative particle, and if in addition the effective mass of the two hadrons $M(K^+ K^-)$ obtained by assigning the kaon mass to each of the hadrons is between 1.005 and 1.035 GeV, the two hadrons are assumed to be the decay products of the $\phi(1020)$ and they are treated as kaons. This procedure is suggested by the distribution of $M(K^+ K^-)$, which shows a clear $\phi(1020)$ signal (see Fig. 16 below). If these hadrons had been assigned (probably erroneously) as pions, they would produce a small bump on the left hand side of the ρ^0 peak.

4.2 Definition of "diffractive sample"

Diffractive events are usually characterized by small values of t and large rapidity gaps in the hadronic final state. Due to the restricted acceptance for hadrons (charged hadrons traveling into the forward region of the cms only, corresponding to 4 units in rapidity at the highest hadronic center of mass energy), rapidity gaps are not suitable in the present experiment for selecting diffractive events: one cannot recognize directly whether a rapidity gap in a reconstructed event is due to the limited acceptance of the detector or to the absence of particles in that rapidity region. However, there is an indirect way of getting information about the activity in the observed rapidity gap region: If no hadron was produced in that region, as expected for a diffractive event, the fraction z of the virtual photon's energy carried by the system of observed hadrons should be close to 1. If hadrons were produced in that region, as expected for an ordinary non-diffractive event, z should be significantly lower than 1.

Fig. 2 shows a plot of t versus z for the inelastic sample. t was determined from the 4-momenta of the virtual photon and the system of observed hadrons. There is a

striking accumulation of events near $z = 1$, strongly correlated with low values of t. This is a clear sign for the presence of diffractive events in the data sample. Low t (or low $t' = t - t_{min}$) and high z will be the main signatures for diffractive events in this analysis.

The subsample of inelastic events satisfying the additional requirements

$$z > z_{cut} = 0.9$$
$$t' < 1 \text{ GeV}^2 \qquad (12)$$
$$Q_H = 0$$

is called the "diffractive sample". Q_H is the observed hadronic net charge. These criteria select predominantly those diffractive events in which all decay particles of the mesonic diffractive system are observed, otherwise z, t' and Q_H, which are calculated from the observed particles only, are unlikely to lie in the kinematic region defined by (12). The selection is very efficient for low diffractive masses ($M_X \lesssim 1$ GeV). It is less efficient for higher masses (see also discussion of Fig. 7 in Sect. 4.3.1): since the rapidity range populated by the decay particles of the diffractive system widens with increasing M_X, the probability of not observing a decay particle also increases. The latter probability also increases because neutral decay particles (which are not considered in this analysis) are more likely to occur at higher M_X.

For the relative normalization of data and Monte Carlo samples (see Sect. 4.3.2) the so-called "extended diffractive sample" is used. It is defined by

$$t' < 1 \text{ GeV}^2$$
$$Q_H = 0 . \qquad (13)$$

The "diffractive sample" is thus obtained from the "extended diffractive sample" by the additional cut in z ($z > z_{cut}$).

The present analysis is restricted to diffractive ρ^0 production. For this reason the "diffractive ρ^0" and "extended diffractive ρ^0" samples are defined. They are obtained from the "diffractive" and "extended diffractive" samples by the additional selections

– no. of accepted hadrons = 2, and
– effective mass of the system of charged (14)
 hadrons between 0.57 and 0.97 GeV.

The numbers of events contained in the various samples and subsamples are compiled in Table 2.

4.3 Correction procedure

The experimental distributions for the diffractive sample have to be corrected for the contamination from non-diffractive events and for the loss of diffractive events. The corrections are performed using the Monte Carlo program described in Section 3.

4.3.1 Data-Monte Carlo comparisons

In the correction procedure it is assumed that non-diffractive production is well described by the Lund

model, and that diffractive production is well described by the model used in the generator GENDIF. In order to test these assumptions, extensive comparisons between experimental data and Monte Carlo data were performed for distributions in event variables (x, Q^2, ν) and hadron variables $(x_F, p_{lab}, p_\perp^h, M_X, z^h, n_{ch})$, both for the "inelastic sample" (which is dominated by non-diffractive events) and the "diffractive sample" (which is dominated by diffractive events).

Examples of data-Monte Carlo comparisons for the inelastic samples are shown for Q^2 and ν in Figs. 3 and 4, for the average charged multiplicity $\langle n_{ch} \rangle$ versus W^2 in Fig. 5 and for the laboratory momentum of charged hadrons in Fig. 6.

For the diffractive samples, comparisons are made in Figs. 7, 8, 9, 10 for the effective mass M_X of the observed hadrons, $t' = t - t_{min}$, the charged multiplicity n_{ch} and the missing mass squared M_m^2 respectively. M_m^2 is the effective mass squared of the system of unobserved particles in the final state as calculated from the four-momenta of the virtual photon, the target proton and the system of observed hadrons. In the case of a diffractive event M_m^2 is equal to the square of the mass M_B of the baryonic diffractive system, provided all decay particles of the mesonic diffractive system are observed. In Figs. 7, 8, 9, 10, the non-diffractive background in the sample of reconstructed Monte Carlo events is represented by stars. The distributions for the experimental data and for the sample of reconstructed Monte Carlo events were normalized to unit area. The distribution for the non-diffractive background in the reconstructed Monte Carlo sample was scaled by the same normalization factor as the distribution for the total reconstructed Monte Carlo sample.

In nearly all cases there is good agreement between the experimental data and the reconstructed MC events. The deviations in the Q^2 distribution (Fig. 3) would be crucial if absolute cross sections were determined from the observed number of events. However, in the present analysis absolute cross sections are measured via ratios r of event numbers, which are then converted into absolute cross sections using the F_2^p measurements from another analysis of this experiment (see Sect. 4.4). The ratios r are quite insensitive to deficiencies in the Monte Carlo simulation.

The region of large t' in Fig. 8 is more populated in the experimental data than in the reconstructed Monte Carlo. This could be an indication for a stronger contribution from double-diffraction dissociation events (larger value of h) in the experimental data than assumed in the Monte Carlo model for diffractive production.

The negative values of M_m^2 (Fig. 10) result from the experimental resolution. The asymmetry of the M_m^2 distribution is mainly due to the non-diffractive background (shown by the distribution with stars), but partly to the contribution from DD events, which by definition have a higher baryonic diffractive mass than the single-diffraction dissociation events. From the sample of reconstructed Monte Carlo events the contribution from DD events in the diffractive sample is estimated to be 10% (see also Fig. 14). Like in Fig. 8, the small excess
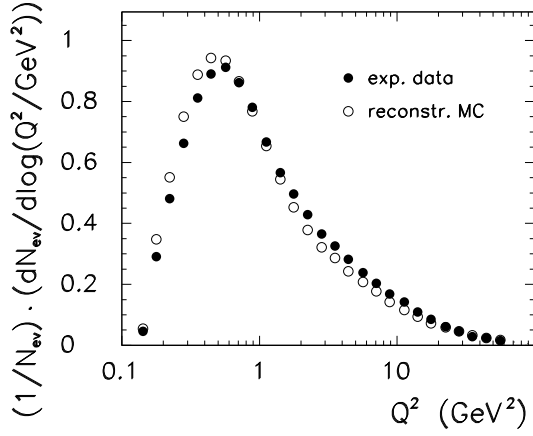
Fig. 3. Q^2 distribution for the inelastic sample: raw data (histogram) and reconstructed Monte Carlo (full circles).
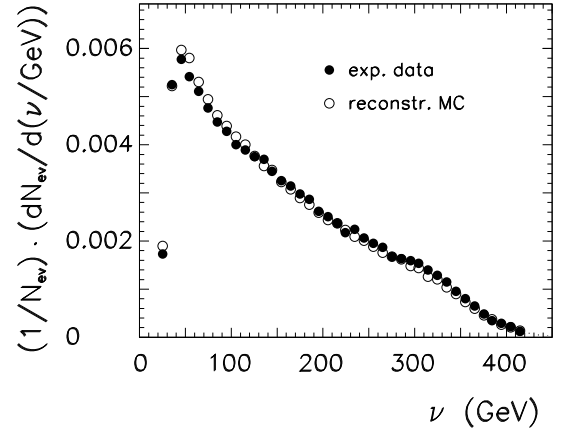

Fig. 4. ν distribution for the inelastic sample: raw data (full circles) and reconstructed Monte Carlo (open circles).
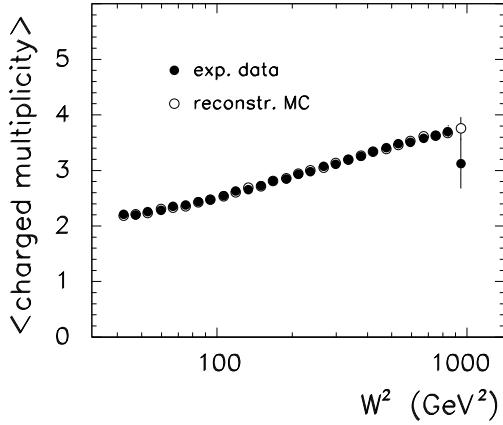

Fig. 5. Average multiplicity of charged hadrons versus W for the inelastic sample: raw data (full circles) and reconstructed Monte Carlo (open circles).
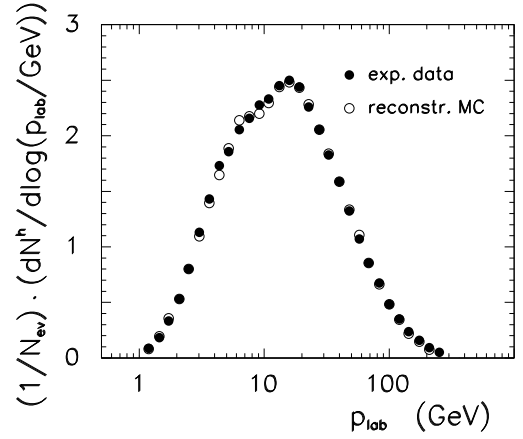

Fig. 6. Normalized distribution $(1/N_{ev}) \cdot (dN^h/d\log(p_{lab}/\mathrm{GeV}))$ of the momentum of charged hadrons in the laboratory frame for the inelastic sample: raw data (full circles) and reconstructed Monte Carlo (open circles).

at $M_m^2 \gtrsim 10$ GeV^2 in the M_m^2 distribution of the experimental data in Fig. 10 suggests that h is in fact larger than assumed in the Monte Carlo model.

From Fig. 7 it is seen that the fraction of non-diffractive events in the sample of reconstructed events depends strongly on M_X. At $M_X \approx 3$ GeV it approaches 100% , making an analysis of higher diffractive masses impossible.

The Monte Carlo data do not reproduce the tail of the $p_\perp^h$ distribution for the inelastic sample (not shown), which is systematically more populated in the experimental data. The discrepancy is partly due to the fact that the parton distribution functions by Donnachie and Landshoff, which are used in the event generation, do not include a gluon distribution function. As a consequence, the photon-gluon-fusion graph is not simulated, which is known to contribute to a widening of the $p_\perp^h$ spectrum [63]. However, since the fraction of high-$p_\perp^h$ hadrons is very low that does not affect any of the quantitative results given here. The discrepancy between data and Monte Carlo at high $p_\perp^h$ is taken into account in the determination of systematic errors in Sect. 4.5.

4.3.2 Relative normalization of data and Monte Carlo samples

In Fig. 11 the data-Monte Carlo comparison is shown for the distribution of z, for the extended diffractive ρ^0 sample. The distributions were normalized to each other in the region $z < z_{norm}$, with $z_{norm} = 0.7$. It can be seen that the Monte Carlo model reproduces the experimental data well, in particular in the region $z < z_{norm}$, where the contribution from diffractive events is low. The width of the peak near $z = 1$ reflects the experimental resolution, which is also well described by the Monte Carlo simulation.

The amount of non-diffractive background in the diffractive ρ^0 sample can be seen from Fig. 12, which shows the distribution of z for the extended diffractive ρ^0 sample in the experimental data (full circles). The background from non-diffractive events is estimated by normalizing the z distribution for the extended diffractive ρ^0 sample of the reconstructed Monte Carlo events to that of the experimental data in the region $z < z_{norm}$, and multiplying the z distribution for the non-diffractive
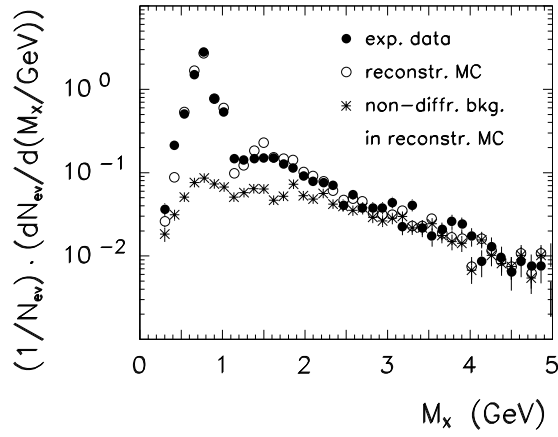
Fig. 7. Distribution of the effective mass M_X of the system of charged hadrons for the diffractive sample: raw data (full circles) and reconstructed Monte Carlo (open circles). The non-diffractive background in the sample of reconstructed Monte Carlo events is represented by stars.

Fig. 8. Distribution of t' for the diffractive sample: raw data (full circles) and reconstructed Monte Carlo (open circles). The non-diffractive background in the sample of reconstructed Monte Carlo events is represented by stars.

Fig. 9. Distribution of the multiplicity n_{ch} of charged hadrons for the diffractive sample: raw data (full circles) and reconstructed Monte Carlo (histogram). $P(n_{ch})$ is defined as the fraction of events with a charged multiplicity equal to n_{ch}. The non-diffractive background in the sample of reconstructed Monte Carlo events is represented by stars.

Fig. 10. Distribution of the missing mass squared M_m^2 for the diffractive sample: raw data (full circles) and reconstructed Monte Carlo (open circles). The non-diffractive background in the sample of reconstructed Monte Carlo events is represented by stars.
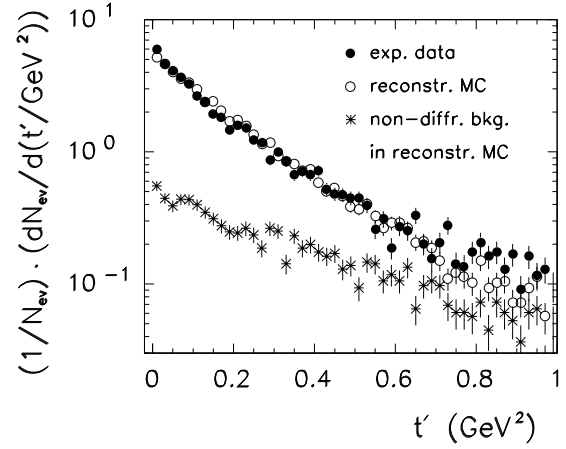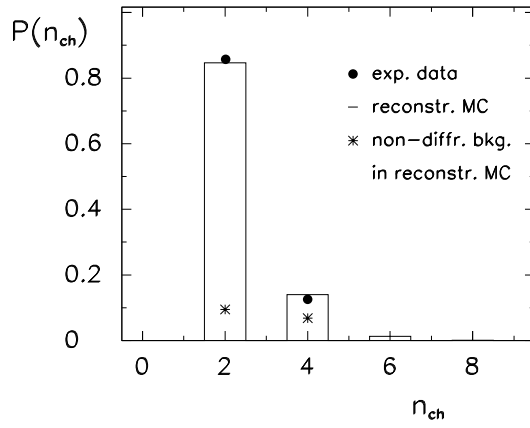
events in the sample of reconstructed Monte Carlo events by the same normalization factor. The resulting distribution is drawn as stars in Fig. 12. One notices that the region $z < z_{norm}$, which is used for the relative normalization of data and Monte Carlo samples, is practically free of diffractive ρ^0 events. The diffractive ρ^0 sample on the other hand, which according to (12) corresponds to the region $z > 0.9$ in Fig. 12, is dominated by diffractive events with a contamination of 7.4% from non-diffractive events.

The shape of the z distributions is different for different regions of the kinematic variables (Q^2, ν, n_{ch}). However, in all cases good agreement was found between the experimental data and the Monte Carlo reconstructed sample in the region $z < z_{norm}$. This confirms the conclusion that non-diffractive production is well described
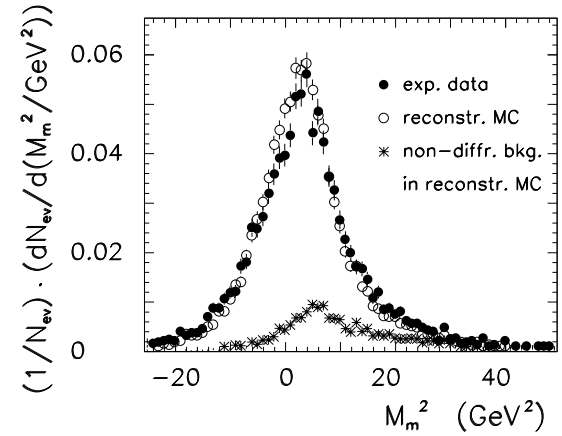
by the Lund model. It can thus be safely used to estimate the non-diffractive background in the diffractive sample.

When correcting a specific distribution $(dN/dv)_{meas}$ in a variable v (which stands for $Q^2, x, \nu, M_X, t', n_{ch}$) for the *diffractive sample*, the relative normalization between data and Monte Carlo events and the estimation of the non-diffractive background in the experimental diffractive sample is actually done using the z distributions in each bin of v separately. In this way a distribution $(dN/dv)_{non-diff}$ is obtained, which is the expected non-diffractive background to the original distribution $(dN/dv)_{meas}$.

4.3.3 Correction of the experimental data

After subtracting $(dN/dv)_{non-diff}$ from $(dN/dv)_{meas}$ the final corrections for the loss of diffractive events (due
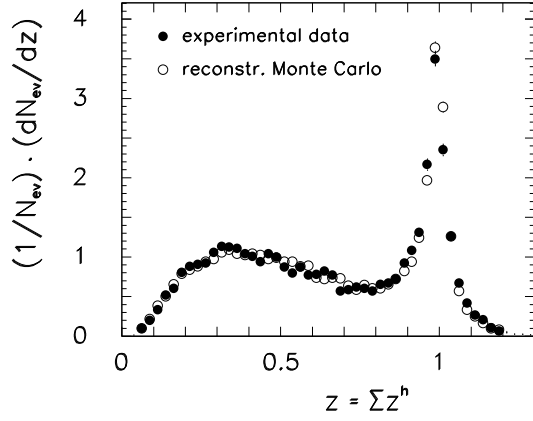
Fig. 11. Distribution of z for the extended diffractive ρ^0 sample: raw data (full circles) and reconstructed Monte Carlo (open circles). The Monte Carlo distribution has been normalized to the data distribution in the region $z < 0.7$.
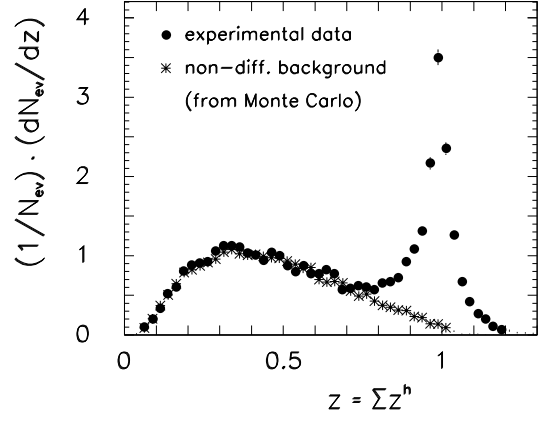

Fig. 12. Distribution of z for the extended diffractive ρ^0 sample: raw data (full circles) and expected background from non-diffractive events (stars). The full-circle distributions in Figs. 11 and 12 are identical.
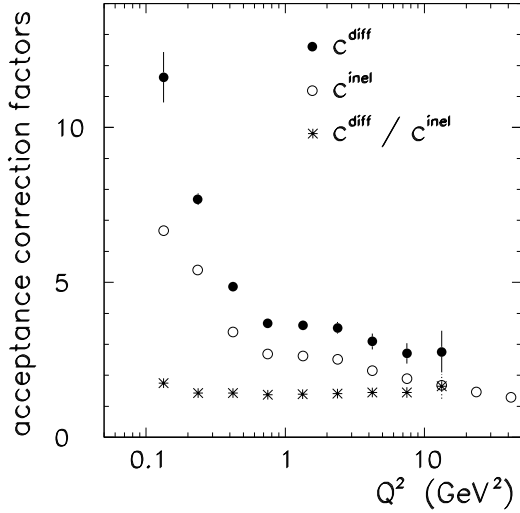

Fig. 13. The acceptance corrections c^{diff} and c^{inel} for diffractive and inelastic events respectively, and the ratio c^{diff}/c^{inel}, as functions of Q^2.

to restricted geometrical acceptance, chamber inefficiencies, trigger and reconstruction losses), for the measurement errors and for radiative effects are performed by applying a multiplicative correction factor $c^{diff}(v)$:

$$(dN/dv)_{corrected} =$$

$$\left[\left(\frac{dN}{dv} \right)_{meas} - \left(\frac{dN}{dv} \right)_{non-diff} \right] \cdot c^{diff}(v) \qquad (15)$$

$$c^{diff}(v) = \frac{(dN/dv)^{diff}_{MC\ true}}{(dN/dv)^{diff}_{MC\ rec}}.$$

$c^{diff}(v)$ is the ratio of the v distribution for the diffractive events in the sample of true Monte Carlo events and the v distribution for the true diffractive events in the "diffractive sample" of the reconstructed Monte Carlo events.

For measuring ratios of diffractive to inelastic cross sections and for determining absolute diffractive cross sections (see Sect. 4.4) also corrected distributions for the inelastic sample are needed. A distribution dN/dV in a variable V (which stands for Q^2, x, ν) for the *inelastic sample* is corrected by applying a multiplicative correction factor

$$c^{inel}(V) = \frac{(dN/dV)^{inel}_{MC\ true}}{(dN/dV)^{inel}_{MC\ rec}} \qquad (16)$$

where $(dN/dV)^{inel}_{MC\ true}$ is the V distribution for the true Monte Carlo events, and $(dN/dV)^{inel}_{MC\ rec}$ the V distribution for the "inelastic sample" of the reconstructed Monte Carlo events.

As can be seen in Fig. 13, both c^{diff} and c^{inel} decrease as Q^2 increases, with typical values of 4.5 and 3 respectively. c^{diff} and c^{inel} also decrease with increasing ν. The ratio c^{diff}/c^{inel} increases with increasing ν and depends only weakly on Q^2. The strong variation of c^{diff} and c^{inel} with Q^2 at low Q^2 reflects the corresponding variation of the overall muon reconstruction efficiency. The latter cancels in the ratio c^{diff}/c^{inel}, which explains the flat behavior of c^{diff}/c^{inel} with Q^2.

Estimates of the non-diffractive background and the DD contribution in the "diffractive ρ^0 sample" are given in Figs. 14 and 15 as a function of Q^2 and t' respectively. They show for reconstructed Monte Carlo events the fraction g of true diffractive events (dashed lines) and the ratio $h = DD/(SD + DD)$ (dotted lines). The fraction g is in the order of 90%, decreasing weakly with increasing Q^2 and t'. The ratio h is independent of Q^2 and it is approximately 10% for $t' < 0.5$ GeV^2, rising towards 55% at $t' = 1$ GeV^2. As compared to the values in the generation (solid lines in Figs. 14 and 15) h is reduced by about a factor of 2. One can conclude that the selections which define the diffractive ρ^0 sample ((12) and (14)) select preferentially SD events and suppress DD events. This is easy to understand, since it is more likely for a DD event to miss a final state particle than for an SD event, leading to lower z in the DD event sample. In addition the cut in t' is more restrictive for the DD than for the SD events. The rise of h with increasing
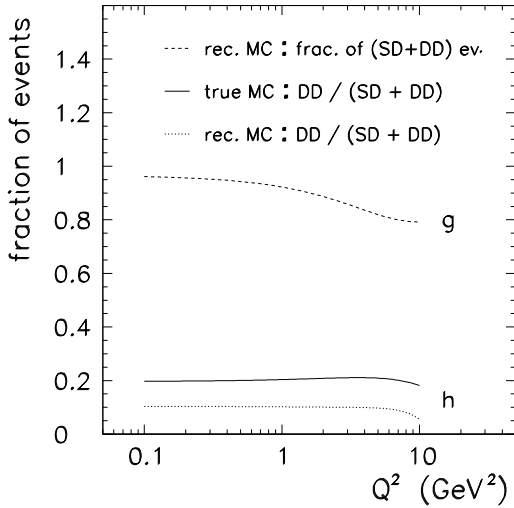
Fig. 14. Fractions of events as a function of Q^2: fraction h of DD events amongst all diffractive ρ^0 events in the MC true sample (solid line); fraction g of true diffractive events in the diffractive ρ^0 sample of the MC reconstructed sample (dashed line); fraction h of DD events amongst all true diffractive events in the diffractive ρ^0 sample of the MC reconstructed sample (dotted line).
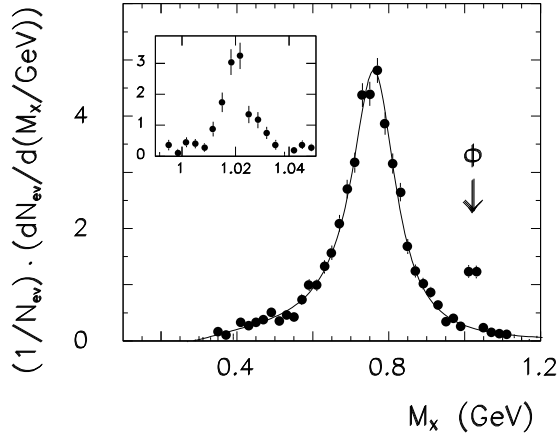

Fig. 16. Distribution of the effective mass M_X of mesonic diffractive systems decaying into two charged hadrons (h^+, h^-) only. The mass distribution in the region 0.99 GeV $< M_X <$ 1.05 GeV ($\phi(1020)$ mass region) is shown with a finer binning in the insert. The solid line represents the result of a fit of expression (20) to the data points outside the ϕ mass region. The errors shown are statistical.

t' in the sample of true Monte Carlo events is due to the flatter average t' slope for the DD as compared to the SD event sample (see Sect. 3).

In section 5 results will be presented which have been corrected either to include or to exclude the full DD contribution. For each quantity to be measured (cross sections, t' slopes, density matrix elements) it will be stated explicitly which of the two options has been chosen.

The single-diffraction ρ^0 reaction is denoted as

$$\mu p \rightarrow \mu \rho^0 p, \tag{17}$$

the double-diffraction ρ^0 reaction as

$$\mu p \rightarrow \mu \rho^0 N', \tag{18}$$
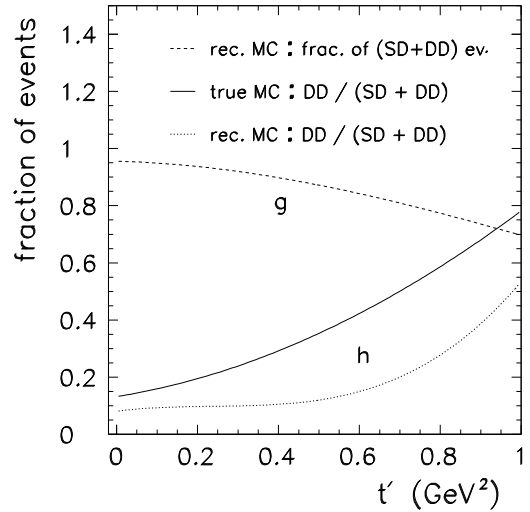

Fig. 15. Fractions of events as a function of t': fraction h of DD events amongst all diffractive ρ^0 events in the MC true sample (solid line); fraction g of true diffractive events in the diffractive ρ^0 sample of the MC reconstructed sample (dashed line); fraction h of DD events amongst all true diffractive events in the diffractive ρ^0 sample of the MC reconstructed sample (dotted line).

where N' is a diffractive baryonic system resulting from the dissociation of a proton.

4.4 Determination of absolute cross sections

Cross sections for diffractive production are determined according to

$$\sigma_{diff} = r \cdot \sigma_{inel}. \tag{19}$$

Here $r = N_{corr}^{diff}/N_{corr}^{inel}$ is the ratio of the corrected number of diffractive events and the corrected number of inelastic events, and σ_{inel} is the absolute μp cross section corresponding to the kinematic region Ω for which N_{corr}^{inel} was measured. σ_{inel} was calculated from the E665 measurements of F_2^p [43], integrating over Ω and averaging over the E665 beam energy spectrum.

The systematic error of σ_{inel} or F_2^p is composed of an overall normalization uncertainty of less than 1.8% and of a kinematics dependent uncertainty [43]. The latter is listed in Table 10 as a function of Q^2 or ν.

4.5 Systematic errors

In the previous Sections the standard procedure for analysing the data was explained. In order to estimate systematic errors the analysis was repeated with certain modifications to the analysis procedure. The following modifications were considered in turn:

a) Remove the E_{big}/ν cut.
b) In the sample of accepted tracks include additional tracks which fulfill the following two conditions: $d < 6$ mm and $\Delta d/d < 6$, where d is the distance of closest approach to the primary vertex.
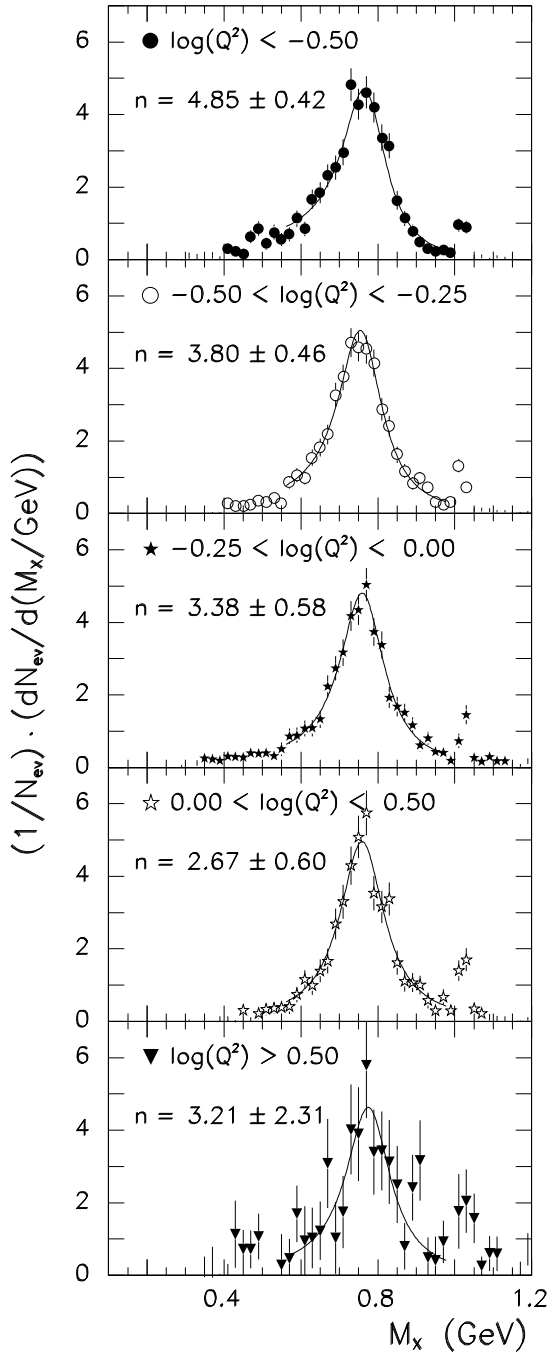c) For a hadron to be accepted require in addition $p_\perp^h < 1$ GeV.

Fig. 17. Distributions of the $h^+ h^-$ effective mass M_X in different regions of Q^2 (in GeV^2). The curves represent the results of the fits of the expression (20) to the mass distributions in the mass range $0.56 \text{ GeV} < M_X < 0.98 \text{ GeV}$. The errors shown are statistical.
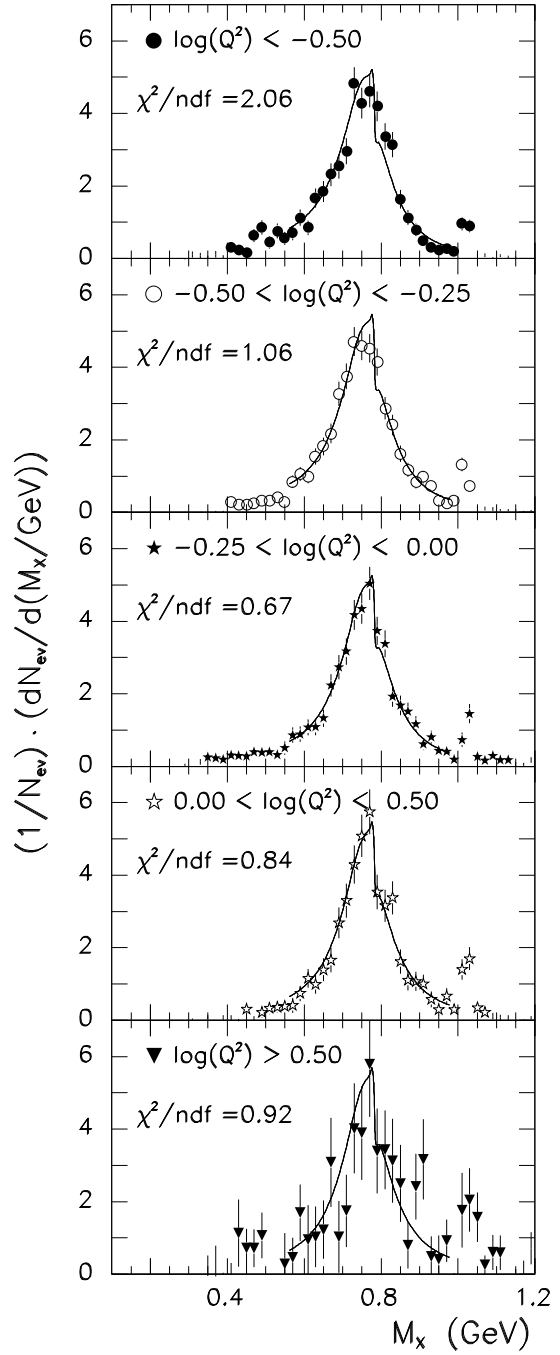
Fig. 18. Distribution of the $h^+ h^-$ effective mass M_X in different regions of Q^2 (in GeV^2). The curves represent the prediction by G. Niesler et al. [67], including the correction term given by eq. (10) of their paper. The χ^2/degrees of freedom for the comparison with the data is given for each Q^2 range. The errors shown are statistical.

d) Instead of the selections $\nu > 20$ GeV and $\Delta\nu/\nu < 0.20$ use $\nu > 30$ GeV and $\Delta\nu/\nu < 0.10$.

e) In the definition of the inelastic sample require ≥ 1 accepted hadron instead of ≥ 2.

f) Use $z_{cut} = 0.95$ instead of 0.9.

g) Instead of using the variable z with z_{cut} and z_{norm}, use the variable $z^R = (z - 1)/\Delta z$ with $z^R_{cut} = -1.5$

and $z^R_{norm} = -3.0$, where Δz is the measurement error of z. This affects the definition of the diffractive sample: $z^R_{cut} = -1.5$ means accepting only those events for which z is not more than 1.5σ below 1. $z^R_{norm} = -3.0$ means using for the normalization between data and Monte Carlo the sample of those events for which z is more than 3σ below 1.

h) Instead of using the variable z with z_{cut} and z_{norm}, use the variable $z^R = (z-1)/\Delta z$ with $z^R_{cut} = -1.0$ and $z^R_{norm} = -3.0$.

Systematic errors were determined by comparing the results for the various options with those obtained using the standard procedure.

The change of the results for the slope parameter b and the spin density matrix elements is less than 1 σ of the respective statistical error, for each of the modifications considered. The overall systematic error for these quantities is estimated to be approximately equal to the statistical error.

The systematic error of the absolute diffractive cross section σ_{diff} is composed of the systematic error on σ_{inel} (see Sect. 4.4) and that on the ratio r. In the ratio r various systematic errors, for example those due to incomplete or deficient simulation of experimental details in the Monte Carlo program and those due to radiative effects, largely cancel. A residual systematic error of r was estimated by varying the definitions of the "inelastic" and/or the "diffractive" samples, as specified by the options a) to h). The result is $\Delta r/r(\text{syst.}) = \pm 5\%$.

The corrections applied to include or exclude the full double-diffraction contribution depend on the fraction $h = DD/(SD + DD)$ of DD events assumed in the Monte Carlo generation. Using the suppression factor 2 of DD relative to SD events in the diffractive ρ^0 sample (Fig. 14), the change of the corrected SD cross section due to a change of h in the Monte Carlo generation can be estimated: changing h from 0.2 to 0.3 (0.4) would imply a relative change of the corrected SD cross section by $\Delta\sigma^{SD}/\sigma^{SD} = -7.4\% \ (-15.7\%)$.

By definition, the corrected (SD+DD) cross section is obtained from the corrected SD cross section by $\sigma^{SD+DD} = \sigma^{SD}/(1-h) = \sigma^{SD}/0.8$. The relative change of the corrected (SD + DD) cross section due to a change of h from 0.2 to 0.3 (0.4) is $\Delta\sigma^{SD+DD}/\sigma^{SD+DD} = 5.9\% \ (12.6\%)$.

The errors drawn in the figures and listed in the tables are statistical only, unless explicitly stated otherwise.

5 Results

Again, throughout the paper "log" denotes the logarithm to the base 10.

5.1 Diffractive mass spectrum

The mass spectrum for mesonic diffractive systems decaying into two charged particles only is shown in Fig. 16. It should be emphasized that the distribution is fully corrected for losses of two-charged-hadron decays of the mesonic diffractive system X. It is not corrected for decays of the mesonic diffractive system which involve neutral particles or more than two charged hadrons. The distribution is corrected to include the full double-diffraction contribution.
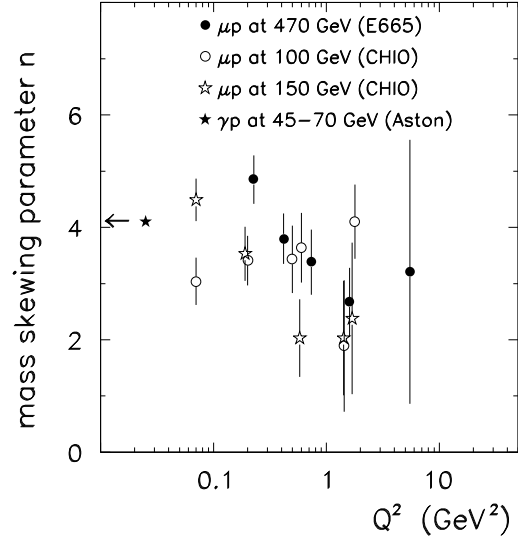

Fig. 19. The mass skewing parameter n as a function of Q^2. The results from this experiment are compared with those from the μp experiment CHIO [22] and the photoproduction experiment [3]. The erros on the E665 points are statistical.

The distribution is dominated by the $\rho^0(770)$ and exhibits also a clear signal of the $\phi(1020)$. The mass distribution in Fig. 16 has been fitted by a superposition of a resonance term BW_ρ for the ρ^0 and a background term BG, excluding the ϕ mass region:

$$\frac{dN}{dM_X} = c \cdot [a \cdot BW_\rho + (1-a) \cdot BG] \qquad (20)$$

$$BW_\rho = \frac{M_X M_\rho \Gamma}{(M_X^2 - M_\rho^2)^2 + (M_\rho \cdot \Gamma)^2} \cdot \left(\frac{M_\rho}{M_X}\right)^n \cdot c_{BW}$$

$$\Gamma = \Gamma_\rho \left(\frac{q}{q_0}\right)^3 \frac{M_\rho}{M_X}$$

$$q = \sqrt{\frac{M_X^2}{4} - M_\pi^2} \ ; \ q_0 = \sqrt{\frac{M_\rho^2}{4} - M_\pi^2}$$

$$BG = (M_X - 2 \cdot M_\pi)^\alpha \exp(\beta M_X) \cdot c_{BG}$$

(all M and Γ are in GeV).

M_ρ is the central mass value and Γ_ρ the width of the ρ^0, M_π is the pion mass, and c_{BW} and c_{BG} are factors determined such that the integrals of BW_ρ and BG over the fit range in M_X are equal to 1. In the fit c, a, M_ρ, Γ_ρ, n, α and β were treated as free parameters. A good fit to the mass distribution is obtained with a χ^2 value of 57.2 for 41 degrees of freedom. The results of the fit are compiled in Table 3. The fitted value of M_ρ is slightly above and that of Γ_ρ is slightly below the corresponding PDG value (769 and 151 MeV respectively). With the specific parametrization chosen in (20), the data do not require a significant contribution from non-resonant diffractive background and the distribution is well reproduced by the ρ^0 contribution alone. 87.6% of the Breit-Wigner distribution lie in the mass region 0.57 GeV $< M_X < 0.97$ GeV.

Fits of expression (20) were also performed to the $\pi^+\pi^-$ mass distributions in different regions of Q^2 (Fig. 17). In this case only the mass region 0.56 GeV $<$
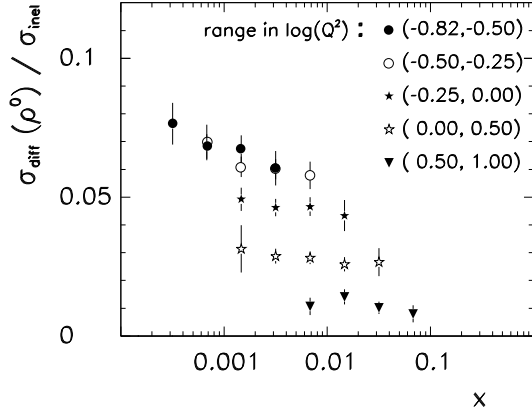
Fig. 20. The ratio $\sigma_{diff}(\rho^0)/\sigma_{inel}$ as a function of x, for different bins of Q^2 (in GeV^2). The errors shown are statistical.

Fig. 21. The ratio $\sigma_{diff}(\rho^0)/\sigma_{inel}$ as a function of ν, for different bins of Q^2 (in GeV^2). The errors shown are statistical.

$M(\pi^+\pi^-) < 0.98$ GeV was considered which contains the main information about the skewness and which is less sensitive to possible background contributions or mis-estimation of it. The background contribution was set to zero ($a = 1$) and Γ_ρ was fixed at 146 MeV, according to the fit to the overall mass distribution in Fig. 16. The results of the fits are listed in Table 4 and superimposed onto the distributions in Fig. 17. There is reasonable agreement in the mass skewing parameter n with the measurements from [22] (see Fig. 19). The values of n from the present experiment exhibit a decrease with increasing Q^2, similar to the results obtained at lower energies [10, 12, 21, 13]. The photoproduction measurement by [3] is consistent with this trend. Models on the skewing of the ρ^0 peak are discussed in [64, 65, 66, 67].

In [67] the mass distribution of diffractively produced $\pi^+\pi^-$ pairs is expressed in terms of the two-pion contribution to the photon spectral function, as given by the pion form factor. The corresponding predictions, normalized to the experimental data in the mass region 0.56 GeV $< M(\pi^+\pi^-) < 0.98$ GeV, are compared with the experimental data in Fig. 18. The sharp drop of the theoretical distribution near $M_X = 782$ MeV is due to ρ-ω interference and it reflects the corresponding behavior of the pion form factor F_π [68]. The skewness of the mass distribution in the ρ^0 mass region, and its decrease with increasing Q^2, are well reproduced by the model. The χ^2/degrees of freedom for the comparison is given in Fig. 18 for each Q^2 range.

The subsequent analysis is restricted to the ρ^0. Cross sections for ρ^0 production will be determined using the results of the Breit-Wigner fits discussed above. The different methods for measuring the ρ^0 cross section proposed in the literature [64, 65, 69] yield results which are consistent with each other at the level of 10-15% [6, 7].
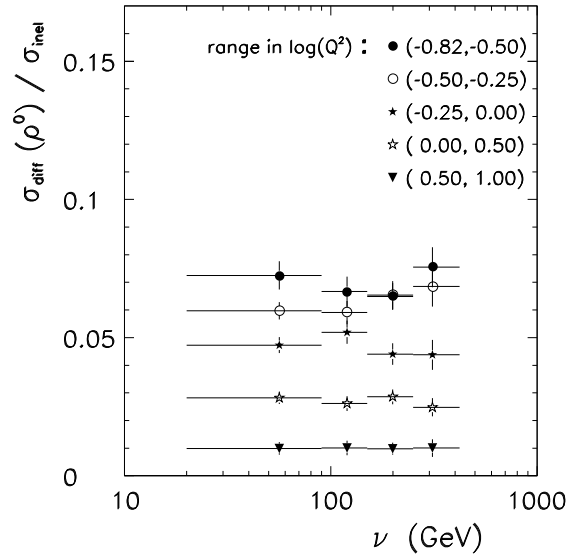
5.2 Cross sections and cross section ratios

In this section cross section measurements for diffractive ρ^0 production are presented. Here "ρ^0" is defined as the mass region 0.57 GeV $< M(\pi^+\pi^-) < 0.97$ GeV, with a correction for the tails of the Breit-Wigner distribution for the ρ^0. The corresponding correction factor is equal to $1/0.876$, which is independent of Q^2 within the experimental errors. The cross sections are for single-diffraction (SD) only, i.e. they were corrected to exclude the contribution from double-diffraction dissociation. The (SD + DD) cross section is obtained from the SD cross section by $\sigma^{SD+DD} = \sigma^{SD}/(1-h) = \sigma^{SD}/0.8$ (see Sect. 4.5).

5.2.1 Ratios of muoproduction cross sections

The corrected ratio $r = \sigma_{diff}(\rho^0)/\sigma_{inel} = \sigma_{diff}(\mu p \to \mu\rho^0 p)/\sigma_{inel}(\mu p \to \mu H)$, where H stands for any hadronic system, is shown for different bins of Q^2 as a function of x in Fig. 20, and as a function of ν in Fig. 21. Essentially Fig. 21 is a different representation of the data points in Fig. 20, since at fixed Q^2 a variation of x corresponds to a variation of ν. There is little or no dependence on x as long as Q^2 is fixed. The x dependence of r, which is of interest in the context of nuclear shadowing, is useful for comparisons with data from heavy nuclear targets.

At fixed Q^2, the ratio r is also quite independent of ν (Fig. 21). On the other hand r depends strongly on Q^2, as can be seen from Fig. 22. At the lowest Q^2 accessible in this experiment diffractive ρ^0 production accounts for about 8% of the inelastic cross section.

5.2.2 Cross sections for virtual-photoproduction of ρ^0 mesons

Following the procedure described in Sect. 4.4, the ratios r were used to calculate absolute cross sections
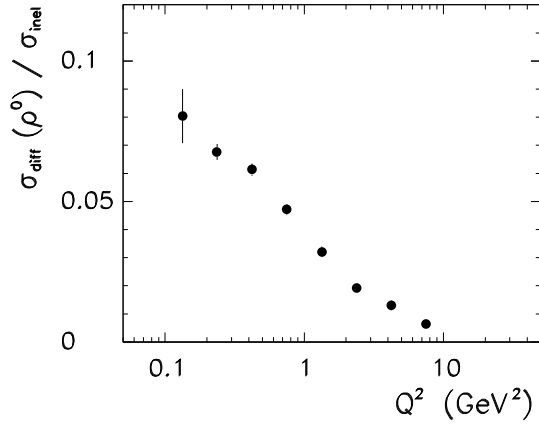
Fig. 22. The ratio $\sigma_{diff}(\rho^0)/\sigma_{inel}$ as a function of Q^2. The errors shown are statistical.

$$d\sigma_{diff}/d\nu dQ^2(\mu p \to \mu\rho^0 p) \tag{21}$$

for diffractive ρ^0 production by muons. The cross sections $\sigma_{diff}(\gamma^* p \to \rho^0 p)$ for diffractive rho production by virtual photons were then obtained according to [70]

$$\sigma_{diff}(\gamma^* p \to \rho^0 p) = \sigma_T + \epsilon \cdot \sigma_L \tag{22}$$

$$= \frac{1}{\Gamma_T} \frac{d\sigma_{diff}(\mu p \to \mu\rho^0 p)}{d\nu dQ^2} .$$

Γ_T is the flux of transversely polarized virtual photons, $\epsilon = \Gamma_L/\Gamma_T$ is the ratio of fluxes of longitudinally to transversely polarized virtual photons (see eqs. (2) and (3)). σ_T (σ_L) is the cross section for diffractive ρ^0 production by transversely (longitudinally) polarized virtual photons.

The results for $\sigma_{diff}(\gamma^* p \to \rho^0 p) = \sigma_T + \epsilon\sigma_L$ as a function of Q^2 are listed in Table 5 and are plotted in Fig. 23. The solid line represents the result of fitting the expression

$$\sigma_{diff}(\gamma^* p \to \rho^0 p) = \sigma_0 \left(\frac{M_\rho^2}{Q^2 + M_\rho^2}\right)^m (1 + \epsilon R) \tag{23}$$

$$R = \frac{\sigma_L}{\sigma_T} = \xi^2 \frac{Q^2}{M_\rho^2} , \tag{24}$$

which is a prediction by the vector dominance model [52, 28], to the E665 data points. In the fit, m was set to 2 and σ_0 and ξ^2 were treated as free parameters. σ_0 may be regarded as an estimate of the photoproduction cross section for diffractive ρ^0 production. Expression (23) yields an excellent fit to the data points with a χ^2/degrees of freedom of 0.86. The fitted values of σ_0 and ξ^2 are $(10.30 \pm 0.33)\mu b$ and (-0.04 ± 0.02) respectively.

The negative value of ξ^2 (and thus of R) shows that expressions (23) and (24) are not a correct representation of the experimental data. More precisely, R as calculated by (24) using the fitted value of ξ^2 cannot be considered as a measurement of σ_L/σ_T. In other high ν ($\nu \gtrsim 50$ GeV) - low Q^2 ($Q^2 \lesssim 10$ GeV^2) leptoproduction experiments, ξ^2 was also found to be close to or compatible
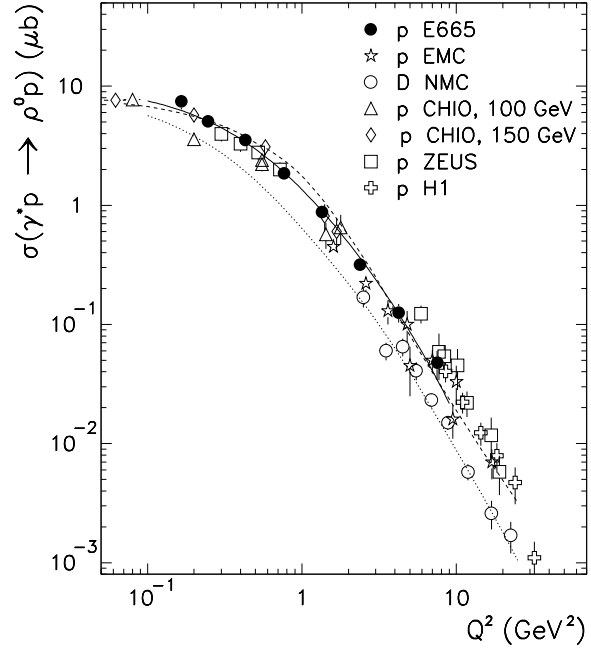
Fig. 23. $\sigma_{diff}(\gamma^* p \to \rho^0 p)$ as a function of Q^2: E665 data (full circles) and the results from the CHIO [22], EMC [24], NMC [26], H1 [16] and ZEUS [15, 17, 18] experiments. The solid line represents the result of fitting expressions (23) and (24) to the E665 data points. The dashed line is a prediction by Pichowsky et al. [38, 39] for $W = 15$ GeV and $\epsilon = 1$. The dotted line is the prediction by J. Nemchik et al. [34] for $W = 15$ GeV and $\epsilon = 1$. The errors on the E665 data points are statistical The numerical values of the E665 data points are listed in Table 5.
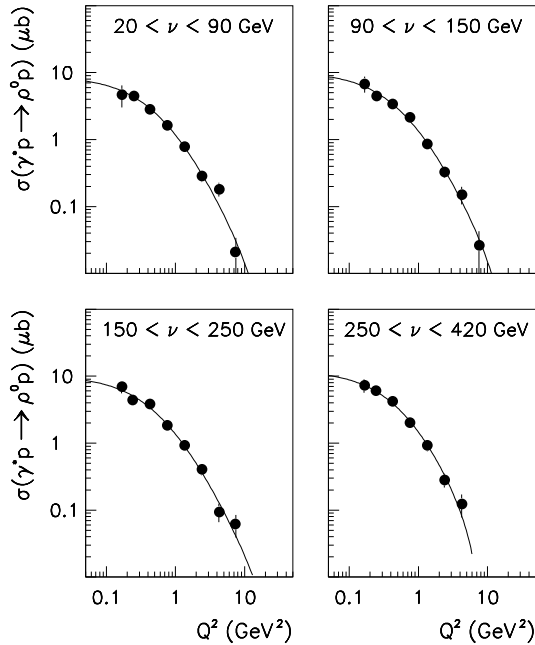
Fig. 24. $\sigma_{diff}(\gamma^* p \to \rho^0 p)$ as a function of Q^2 in different regions of ν. The solid lines represent the results of fitting expressions (23) and (24) to the E665 data points in each ν bin. The errors shown are statistical. The numerical values of the E665 data points are listed in Table 5.
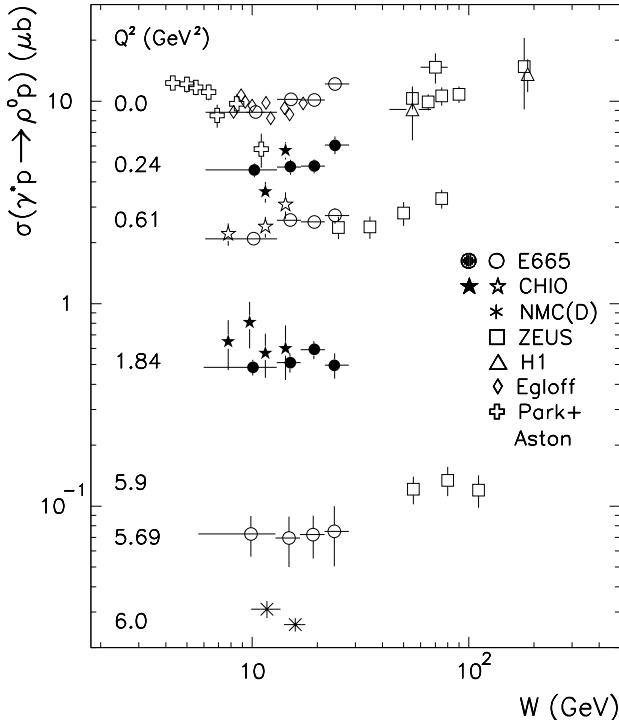
Fig. 25. $\sigma_{diff}(\gamma^* p \to \rho^0 p)$ as a function of W in different ranges of Q^2. The numbers in the plot denote the approximate values of Q^2. The data in the various Q^2 ranges are alternately represented by open and full symbols. The data for $Q^2 > 0$ are from this experiment (E665, circles), from the CHIO [22], the NMC [26, 27] and the ZEUS [15, 17, 18] experiments. The photoproduction data ($Q^2 = 0$) are from [1, 2, 3] and from the ZEUS [5, 6, 9] and H1 [7] experiments. The E665 data points at $Q^2 = 0$ represent the extrapolated cross sections σ_0. The errors on the E665 data points are statistical. The numerical values of the E665 data points are listed in Tables 5 and 6.

with zero [20, 22, 23] when determined from the cross section measurements using (23) and (24). Higher values of ξ^2 are measured at lower ν [11, 12, 21]. A determination of R from the ρ^0 decay angular distributions using s-channel helicity conservation is presented in Sect. 5.4.

The E665 data points in Fig. 23 were also used to determine the power m in (23). For this purpose the data points were fit by the expression (23), in which R was set equal to $R(Q^2)$ as determined from the angular distributions (see eq. (35)). The fit yielded $\sigma_0 = (10.23 \pm 0.56)$ μb and $m = 2.51 \pm 0.07$ with a ξ^2/ndf of 0.40. A comparison with the previous fit, in which m was set to 2 and the parametrization (24) with ξ^2 as a free parameter was used, shows that the extrapolated cross sections agree within the statistical errors.

A prediction for $\sigma_{diff}(\gamma^* p \to \rho^0 p)$ based on a Pomeron-exchange model [38, 39] (dashed line in Fig. 23) appears to describe the Q^2 dependence of the cross section satisfactorily.

A prediction [34] based on the color dipole BFKL model, which provides a unified description of soft and hard deep inelastic phenomena, is drawn as dotted line in Fig. 23. The prediction of the model, in which the photoproduction cross section is calculated as $\sigma_0 = 10.1$

μb, is lower than the E665 measurements in the region 0.15 GeV$^2 < Q^2 < 10$ GeV^2 by about a factor of 2.

Also shown in Fig. 23 are measurements by the CHIO [22], EMC [24], NMC [26], H1 [16] and ZEUS [15, 17, 18] experiments. The data from [18] are preliminary. In general there is good agreement between the experiments, with the exception of the NMC data points, which are systematically lower. Differences between the various results may be due to different definitions of the ρ^0, different treatment of double-diffraction dissociation, different average values of ϵ and different ranges of ν. For the ν (or W) dependence at fixed Q^2 see Fig. 25.

Fig. 24 shows the Q^2 dependence of $\sigma_{diff}(\gamma^* p \to \rho^0 p)$ for different ranges of ν. In each bin of ν the data are well represented by expressions (23) and (24) (solid lines). The results for σ_0 and ξ^2 from fits to the data are compiled in Table 5. There is good agreement between the extrpolated cross sections σ_0 from this experiment and the photoproduction measurements by [2], $\sigma = (9.2 \pm 0.2)\mu b$ for $30 < \nu < 180$ GeV, and [3], $\sigma = (9.2 \pm 0.1)\mu b$ for $20 < \nu < 70$ GeV (see also Fig. 26).

A different representation of the diffractive ρ^0 cross section is given in Fig. 25, in which $\sigma_{diff}(\gamma^* p \to \rho^0 p)$ is plotted versus W ($W^2 = M_p^2 + 2M_p\nu - Q^2$), in different regions of Q^2. W is the invariant mass of the system formed by the virtual photon and the target proton. The numerical values of the E665 data points are listed in Table 6.

The W dependence of the cross section σ_{diff} for some selected values of Q^2 is also shown in Fig. 26. The photoproduction data are compared with the theoretical prediction for a "soft Pomeron" [71, 72], given by the dashed curve. The model reproduces the general trend of the data. At each Q^2 the E665 data points were fitted by a dependence $(W/\text{GeV})^\kappa$, yielding $\kappa = 0.31 \pm 0.20$ at $Q^2 = 0$, $\kappa = 0.31 \pm 0.20$ at $Q^2 = 0.61$ GeV^2 and $\kappa = 0.02 \pm 0.75$ at $Q^2 = 5.69$ GeV^2 (solid curves). At $\langle Q^2 \rangle = 0.48$ GeV^2 the ZEUS experiment [17] obtained $\kappa = 0.33 \pm 0.14$ (stat.) ± 0.15 (syst.). The dotted curves represent the function $(W/\text{GeV})^{0.22}$ (with arbitrary normalization), which is the typical high-energy behavior in soft Pomeron models. Taking into account the systematic errors which are not yet included in the error bars, 20% for E665 and $^{+7}_{-19}$% for ZEUS (at $Q^2 = 5.9$ GeV^2), the E665 and ZEUS data are consistent with a gentle increase of σ_{diff} with W, as expected by models based on soft pomeron exchange. The NMC cross sections, which have an additional systematic error of 20%, tend to be lower than the E665 data (see also Fig. 23).

The x dependence of $\sigma_{diff}(\gamma^* p \to \rho^0 p)$ is shown in Fig. 27 for different regions of Q^2. In each Q^2 range the cross sections appear to decrease with increasing x. However, since in a given Q^2 range the average Q^2 increases by about a factor 2 - 3 when x is varied between its minimum and maximum value, the apparent decrease of the cross section is at least partly due to a reflection of the strong dependence on Q^2 (see Fig. 23). The same remark applies to Figs. 29 and 30. It does not apply to Fig. 25, since in a given Q^2 range the average Q^2 is practically independent of W.
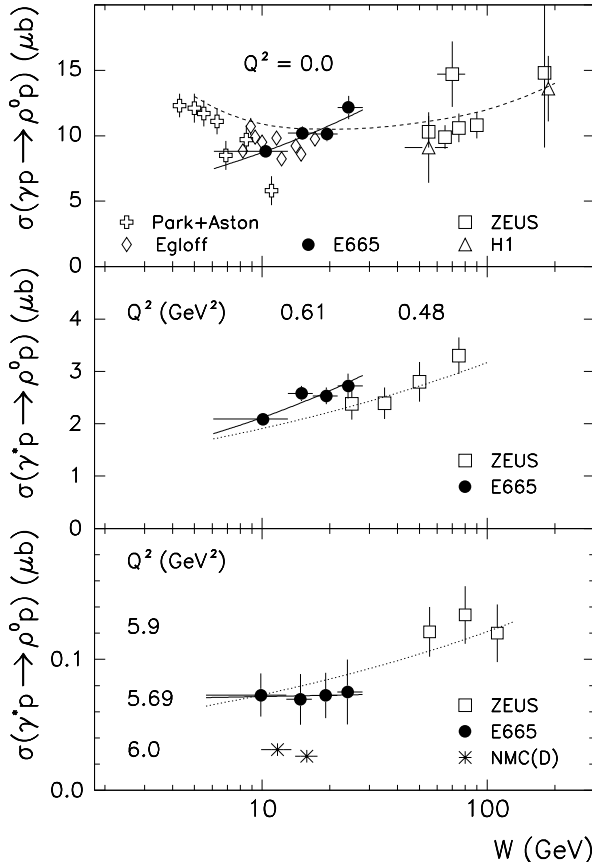
Fig. 26. Cross section for diffractive ρ^0 production by real (upper plot) and virtual (lower plots) photons as a function of W. The photoproduction data are from [1, 2, 3] and from the ZEUS [5, 6, 9] and H1 [7] experiments. The E665 data points at $Q^2 = 0$ represent the extrapolated cross sections σ_0. The data at $Q^2 > 0$ are from this (E665), the NMC [26, 27] and the ZEUS [15, 17, 18] experiments. The solid curves represent the results of fits of the expression $a \cdot (W/\text{GeV})^\kappa$ to the E665 data points. The dashed curve is the prediction from [71, 72]. The dotted curves represent the function $(W/\text{GeV})^{0.22}$ with arbitrary normalization. The errors on the E665 data points are statistical. The numerical values of the E665 data points are listed in Tables 5 and 6.

Using $R = \sigma_L/\sigma_T$ as determined in Sect. 5.4 from the angular distributions, the transverse and longitudinal cross sections σ_T and σ_L have been derived from $\sigma_{diff}(\gamma^* p \to \rho^0 p)$ according to

$$\sigma_T = \frac{\sigma_{diff}}{1 + \epsilon R} \qquad \sigma_L = \frac{\sigma_{diff}}{\frac{1}{R} + \epsilon} . \qquad (25)$$

When applying (25) to the epxerimental data the variation of R and ϵ with the kinematic quantities has been taken into account by computing R and ϵ in each bin separately. R was calculated using (35). For ϵ the weighted average $\langle \epsilon \rangle_1 = \int \epsilon \sigma_L \cdot d\nu dQ^2 / \int \sigma_L \cdot d\nu dQ^2$ was taken, where σ_L was parametrized according to (23), with $m = 2.51$ and $R(Q^2)$ from (35).

σ_T, σ_L and $(\sigma_T + \sigma_L)$ are displayed as a function of Q^2 in Fig. 28, and tabulated in Table 7. In the Q^2 range 0.15 - 10 GeV^2, the Q^2 dependence of σ_L is clearly weaker than that of σ_T , as expected from the strong rise of R in this Q^2 region (see Fig. 41). σ_T is dominating at low Q^2, and σ_L starts exceeding σ_T at $Q^2 \approx 2$ GeV^2.
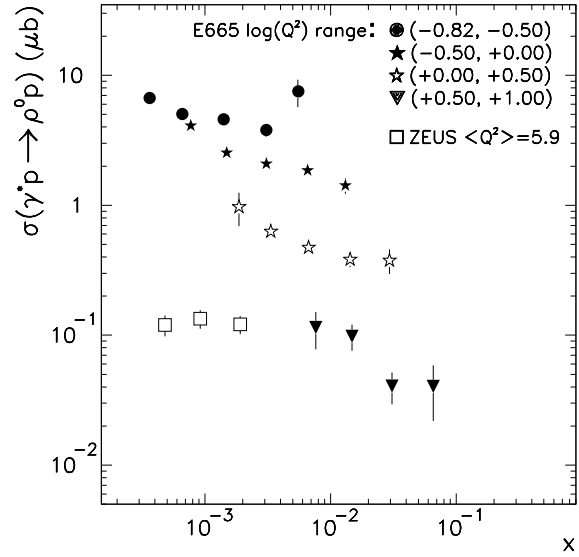
Fig. 27. $\sigma_{diff}(\gamma^* p \to \rho^0 p)$ as a function of x in different bins of Q^2 (in GeV^2). The preliminary data from [18] are shown for comparison. The errors on the E665 data points are statistical. The numerical values of the E665 data points are listed in Table 9.
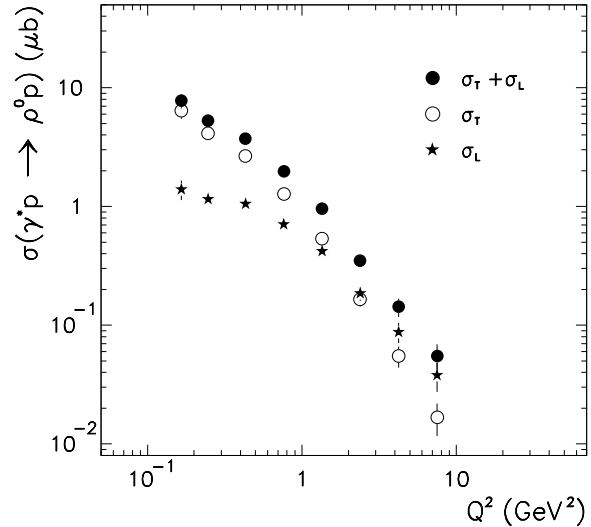
Fig. 28. The cross sections σ_T, σ_L and $\sigma_T + \sigma_L$ for diffractive ρ^0 production by virtual photons on protons, as a function of Q^2. The errors shown are statistical. The numerical values of the E665 data points are listed in Table 7.

Assuming R to depend only on Q^2, σ_T and σ_L can be determined as a function of W or x in different Q^2 ranges. The results for $(\sigma_T + \sigma_L)$ as a function of W are tabulated in Table 8. The results for σ_T and σ_L as a function of x in different regions of Q^2 are plotted in Fig. 29 and 30 respectively and are listed in Table 9.

In Table 10 the average values of Q^2, ν, W, x and ϵ are given for the different bins in log (Q^2/GeV^2) or ν. The average of a quantity v was determined as $\langle v \rangle = \int v \sigma_{diff} \cdot d\nu dQ^2 / \int \sigma_{diff} \cdot d\nu dQ^2$, where σ_{diff} was parametrized according to (23) with $m = 2.51$ and $R(Q^2)$ from (35). It can be seen that x and Q^2 are

Fig. 29. The cross section σ_T as a function of x for different regions of Q^2 (in GeV^2). The errors shown are statistical. The numerical values of the E665 data points are listed in Table 9.

Fig. 30. The cross section σ_L as a function of x for different regions of Q^2 (in GeV^2). The errors on the E665 data points are statistical. The numerical values of the E665 data points are listed in Table 9.
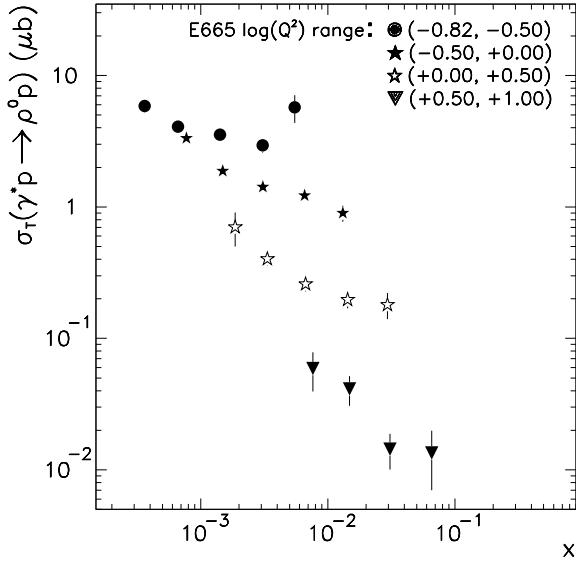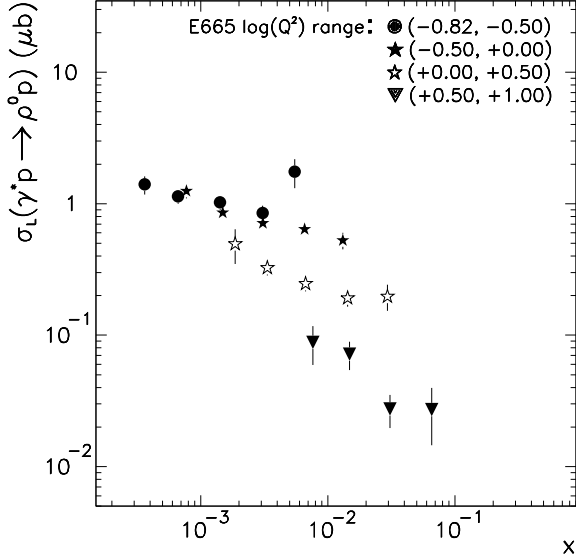
strongly correlated, whereas ν (or W) and Q^2 are practically uncorrelated. ϵ is nearly independent of Q^2 and decreases with increasing ν at high ν.

5.3 Distributions of t' and $p_\perp^2$

As has been shown in Sect. 4.3 (Fig. 15) the t' distributions are particularly sensitive to the presence of DD events. In order to study the influence from DD, the t' distributions have been corrected to exclude or include the full DD contribution. Note that in both cases the
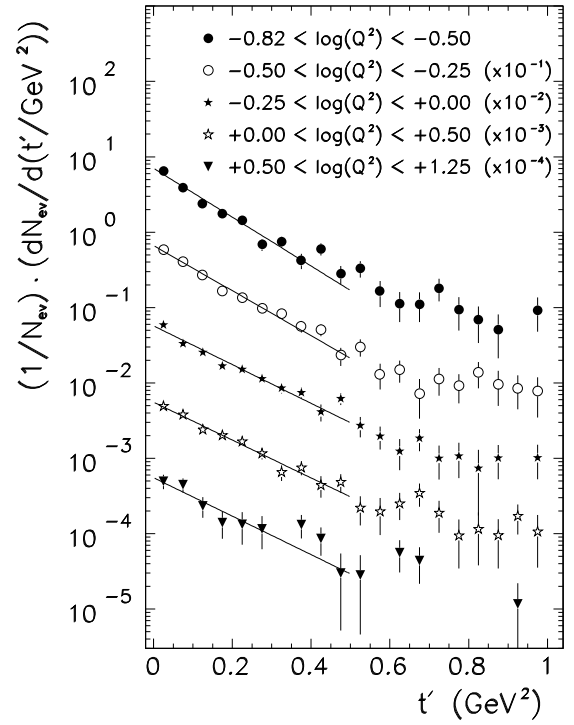
Fig. 31. t' distributions in different regions of Q^2 (in GeV^2), corrected to exclude the full double-diffraction contribution. The solid lines represent the results of fits of expression (26) to the experimental distributions. The results of the fits are listed in Table 11 (parameter b in column labelled SD). The errors shown are statistical.

corrections depend on the simulation of DD events in the Monte Carlo program, because there is no clean way in the present experiment of separating the DD events. The results for the slope values b obtained from fits of the expression

$$\frac{d\sigma}{dt'} = A e^{-bt'} \qquad (26)$$

to the corrected distributions are listed in Table 11.

The various fits differ in the t' range used for the fit, in the Q^2 range and in the treatment of the DD contribution. In general the slope values b are lower by ~ 0.7 GeV^{-2} if the DD contribution is included. The same trend is seen in the sample of true Monte Carlo events. The slope values also decrease as the upper limit in t' is increased, typically by 0.5 GeV^{-2} when changing the upper limit from $t' = 0.5$ GeV^2 to 1.0 GeV^2. This behavior is explained by the rising relative contribution of DD events with increasing t' (Fig. 15). The t' range which is most appropriate for the determination of the SD corrected slopes is the range $t' < 0.5$ GeV^2, because the corrections for the DD contribution are small in this region and start increasing only above $t' = 0.5$ GeV^2.

There is a clear decrease of the slope value with increasing Q^2: b drops by ~ 2 GeV^{-2} in the Q^2 range from 0.15 to 3 GeV^2 (Figs. 31, 32). This behavior is also present in the uncorrected data, however, not in the Monte Carlo samples.

Fig. 32. The slope parameter b as a function of Q^2 from different muoproduction experiments: The data are from this experiment (full circles), and from [20], CHIO [22] and NMC [26]. Photoproduction measurements [3, 4] are shown for comparison. The errors on the E665 points are statistical.

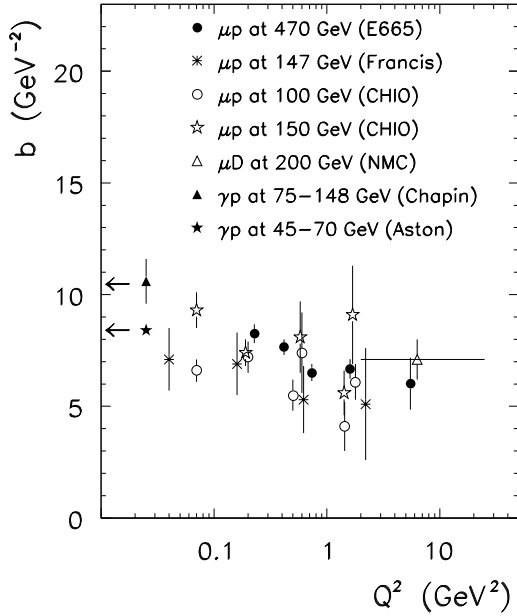In the experimental data t_{min} is calculated assuming the baryonic diffractive mass M_B to be equal to the proton mass. This leads to additional experimental smearing in t' in double-diffraction dissociation events [25]. For this reason the same analysis as for t' was done with the variable $p_\perp^2$, which is the square of the transverse momentum (relative to the direction of the virtual photon in the cms) of the mesonic diffractive system X. The corresponding results are included in Table 11.

The same conclusion as obtained for the slopes b can be drawn for the slopes d of the $p_\perp^2$ distributions. In particular also the Q^2 dependence is observed when the variable $p_\perp^2$ is used. This indicates that the smearing effects are properly taken into account in the correction procedure. It should be noted that the values of d and b are not expected to be identical. At small production angles of the diffractive system in the cms, t' and $p_\perp^2$ are related by

$$t' \approx \frac{p}{p'} p_\perp^2 , \qquad (27)$$

where p and p' are the cms momenta of the virtual photon and the mesonic diffractive system respectively. The expected ratio b/d of slope values is thus equal to p'/p which is different from 1 and which depends on ν, Q^2, M_X and M_B. However, in the kinematic range considered in this analysis, b/d is close to 1, the difference being negligible compared to the experimental errors. This was verified by Monte Carlo calculations.

In Fig. 32 the slope values b are compared with the results from other muoproduction experiments, which cover a similar region in ν and Q^2 [20, 22, 26]. The differences between the results of the various experiments may be partly due to the different experimental procedures,

such as the t' range used in the fit and the corrections applied for the non-diffractive and double-diffraction dissociation background. The data within each of the experiments is consistent with a moderate fall-off of b with increasing Q^2. The slope parameters as measured in this experiment tend to be lower than those measured in photoproduction in a similar ν range: $b = (8.4 \pm 0.1)$ GeV^{-2} [3] and $b = (10.6 \pm 1.0)$ GeV^{-2} [4]. The decrease of b with increasing Q^2 is usually interpreted as evidence for a shrinkage of the effective $\gamma^* p$ interaction radius [73, 74]. Such a shrinkage was also suggested by the measurements of the diffractive ρ^0 cross section on heavy nuclei [75]. Evidence for a decrease of b with increasing Q^2 has also been seen in experiments at lower [21, 13, 14] and at higher ν [17, 18, 19].

In the ν range covered by this experiment no dependence of b on ν is observed. However, a comparison of b values from E665, $b = (7.7 \pm 0.4)$ GeV^{-2} for $20 < \nu < 420$ GeV and $\langle Q^2 \rangle = 0.43$ GeV^2, and from ZEUS [17], $b = (9.3 \pm 0.7 \text{ (stat.) } \pm 0.8 \text{ (syst.)})$ GeV^{-2} for $1330 < \nu < 4317$ GeV and $\langle Q^2 \rangle = 0.48$ GeV^2, is consistent with the shrinkage of the t distribution expected in the Regge theory with a soft Pomeron ($\alpha' = 0.25$ GeV^{-2}):

$$b_{\text{high } W} - b_{\text{low } W} = 2\alpha' \ln \left(\frac{W_{\text{high}}^2}{W_{\text{low}}^2} \right) \approx 2 \text{ GeV}^{-2} . \qquad (28)$$

A similar shrinkage is observed in photoproduction of ρ^0 mesons [3, 6, 7], and also at higher Q^2 ($8 < Q^2 < 50$ GeV^2) [19]. The shrinkage of the t distribution with increasing W is discussed in the framework of QCD in [76].

5.4 Production and decay angular distributions

The production and decay of the ρ^0 is studied in terms of the following angles [77, 12]:

- ϕ: the azimuthal angle around the direction of the virtual photon in the cms between the lepton plane (formed by the incident and the scattered muon) and the ρ^0 production plane (formed by the virtual photon and the ρ^0);
- ϑ, φ: the polar and azimuthal angles of the decay π^+ in the ρ^0 rest frame respectively: ϑ is the angle between the decay π^+ and the direction of the ρ^0 in the cms (reference axis), φ is the azimuthal angle around the reference axis between the decay plane (formed by the decay π^+ and the reference axis) and the ρ^0 production plane (formed by the virtual photon and the reference axis).
- $\psi = \varphi - \phi$

The angular distributions are shown in Figs. 33, 34, 35, 36 for different regions of Q^2. There is a striking change with Q^2 of the shape of the distributions for $\cos \vartheta$ and ψ, which will be discussed below.

By integrating the theoretical angular distribution $W(\cos \vartheta, \varphi, \phi)$ one obtains the distributions in the variables $\cos \vartheta$, φ and ψ:

Fig. 33. The distribution of $\cos\vartheta$ in different regions of Q^2. The solid lines represent the results of fits of expression (29) to the experimental distributions. The average values of Q^2 are in GeV^2. The errors shown are statistical.
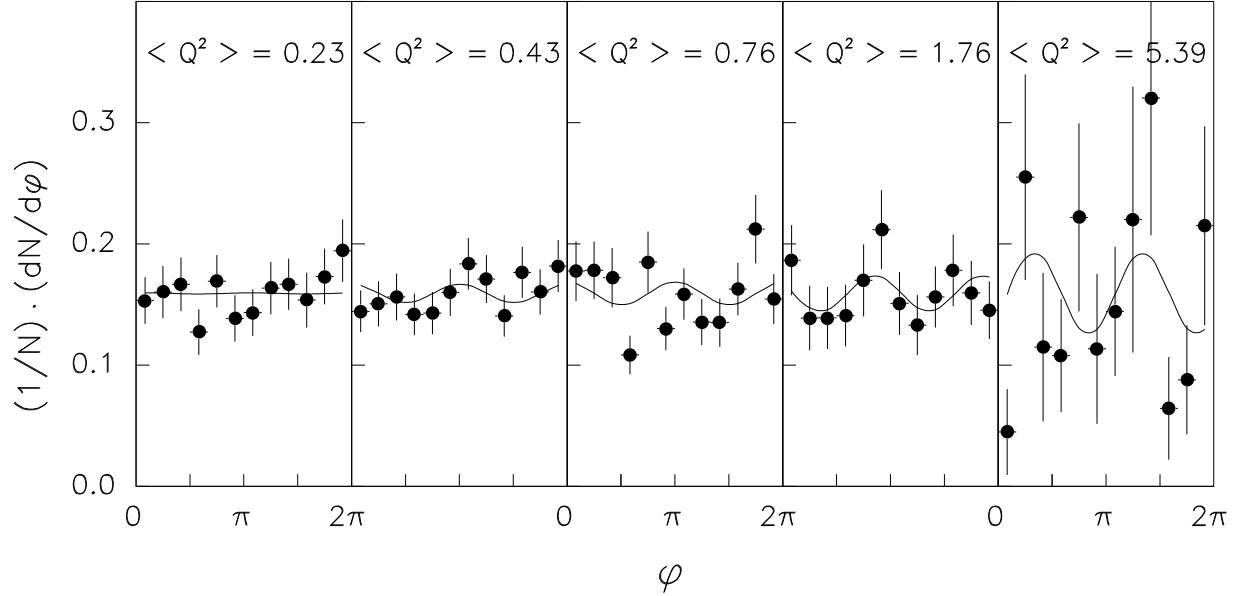
Fig. 34. The distribution of φ in different regions of Q^2. The solid lines represent the results of fits of expression (30) to the experimental distributions. The average values of Q^2 are in GeV^2. The errors shown are statistical.

$$\frac{dN}{d\cos\vartheta} \approx \frac{3}{4}\left\{1 - r^{04}_{00} + \left(3r^{04}_{00} - 1\right)\cos^2\vartheta\right\} \tag{29}$$

The density matrix element r^{04}_{00} is the probability that the ρ^0 has helicity 0 (longitudinal polarization).

$$\frac{dN}{d\varphi} \approx \tag{30}$$

$$\frac{1}{2\pi}\left\{1 - 2r^{04}_{1-1}\cos 2\varphi + P\sqrt{1-\epsilon^2}\,2Im\left(r^3_{1-1}\right)\sin 2\varphi\right\},$$

where ϵ is given by (3) and P is the polarization of the incident muon. The hypothesis that the helicity of

the virtual photon is retained by the ρ^0 is called s-channel helicity conservation (SCHC). If SCHC is assumed $W(\cos\vartheta, \varphi, \phi)$ reduces to $W(\cos\vartheta, \psi)$. After integration over $\cos\vartheta$ one obtains:

$$\frac{dN}{d\psi} \approx \frac{1}{2\pi}\left\{1 + 2\epsilon r^1_{1-1}\cos 2\psi\right\} \tag{31}$$

The density matrix elements r^{04}_{00}, r^{04}_{1-1}, $Im(r^3_{1-1})$ and r^1_{1-1} were determined by fitting the expressions (29), (30) and (31) to the experimental distributions. The distribution of the polarization P in the present experiment has
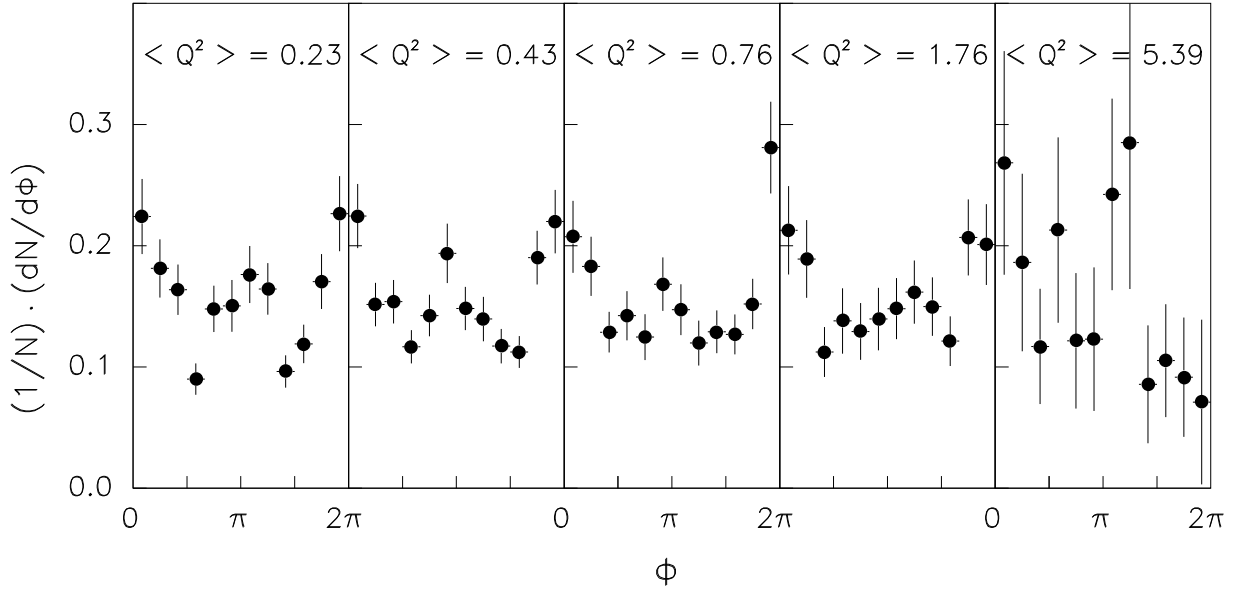
Fig. 35. The distribution of ϕ in different regions of Q^2. The average values of Q^2 are in GeV^2. The errors shown are statistical.
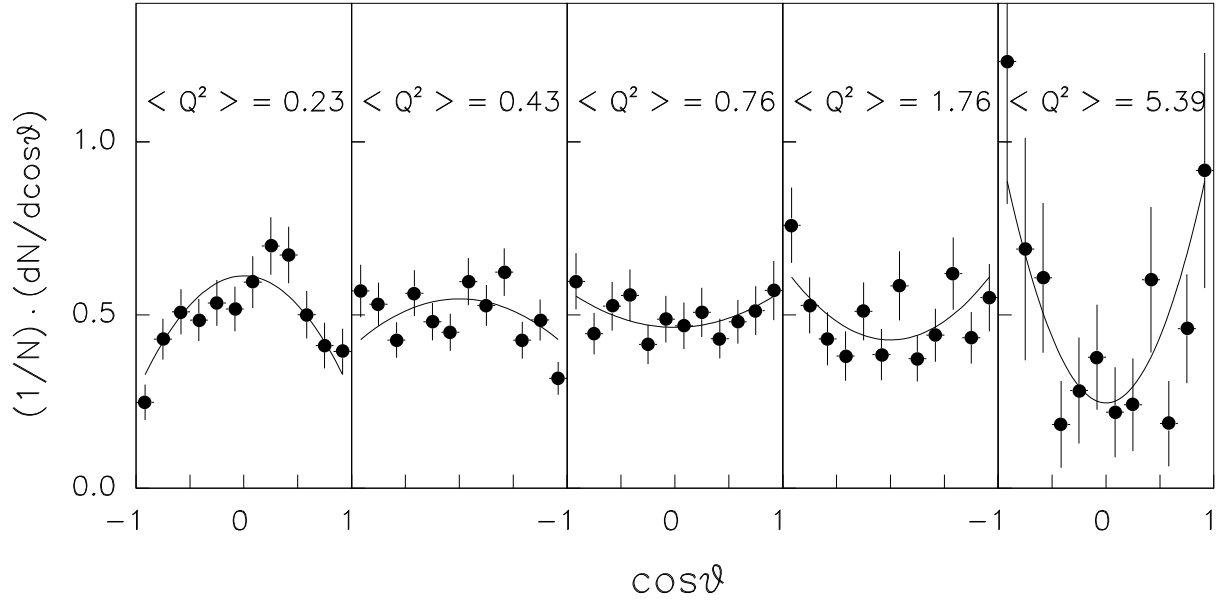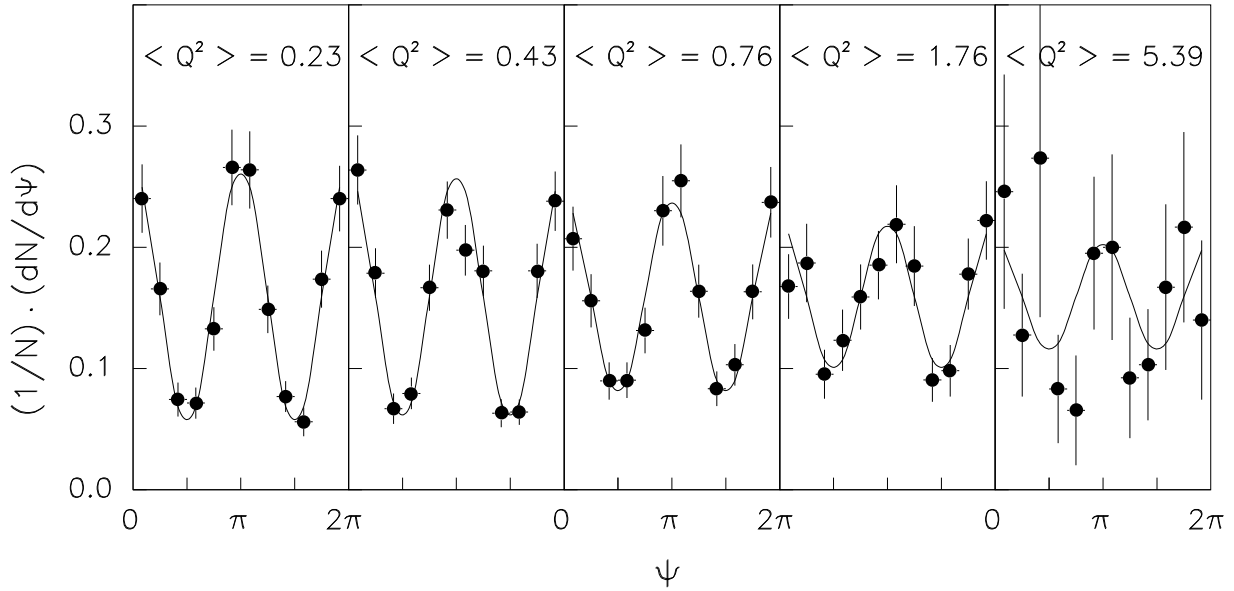

Fig. 36. The distribution of ψ in different regions of Q^2. The solid lines represent the results of fits of expression (31) to the experimental distributions. The average values of Q^2 are in GeV^2. The errors shown are statistical.

a mean of 0.7 and a root mean square deviation of 0.3 [78]. In (30) P was set to 0.7.

For ϵ in (30) and (31) the weighted average $\langle \epsilon \rangle_2$ $= \int \epsilon \Gamma_T \sigma_L \cdot d\nu dQ^2 / \int \Gamma_T \sigma_L \cdot d\nu dQ^2$ was taken, where σ_L was parametrized according to (23) with $m = 2.51$ and $R(Q^2)$ from (35). The weight $\Gamma_T \sigma_L$ was chosen because the (acceptance corrected) number of experimental events, which is used for determining the density matrix elements, is proportional to the muoproduction cross section (21) and not to the cross section $\sigma_{diff}(\gamma^* p \to \rho^0 p)$. Note that $\langle \epsilon \rangle_2$ is different from $\langle \epsilon \rangle_1$ used in the conversion of σ_{diff} into σ_L and σ_T (eq. (25)).

The measured values of r^{04}_{00}, r^{04}_{1-1}, $Im(r^3_{1-1})$ and r^1_{1-1} are plotted as a function of Q^2 in Figs. 37, 38, 39, 40 respectively. The numerical values are listed in Table 12. The data from the present experiment confirm the rapid change of the ρ^0 polarization in the low-Q^2 region [12, 21, 13]: while the fraction of longitudinally polarized ρ^0, given by the value of r^{04}_{00}, is zero at $Q^2 = 0$ [3] it becomes 50% at $Q^2 \approx 2$ GeV^2 (Fig. 37), rising further at higher Q^2.

There seems to be only little dependence of r^{04}_{00} on ν, as can be seen from the data points of the DESY $(2.0 < \nu < 4.5$ GeV), E665 $(20 < \nu < 420$ GeV) and

Fig. 37. The spin density matrix element r_{00}^{04} as a function of Q^2. Previous measurements from DESY [12], EMC [23], NMC [26], ZEUS [15, 17] and H1 [16] are shown for comparison. The errors on the E665 data points are statistical. The numerical values of the E665 data points are listed in Table 12.
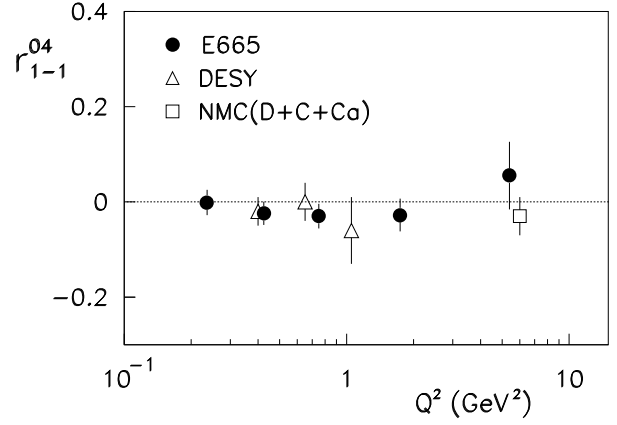
Fig. 38. The spin density matrix element r_{1-1}^{04} as a function of Q^2. Previous measurements from DESY [12] and NMC [26] are shown for comparison. The errors on the E665 data points are statistical. The numerical values of the E665 data points are listed in Table 12.
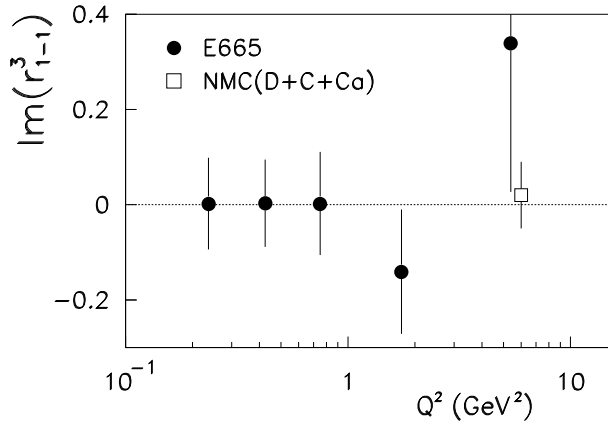
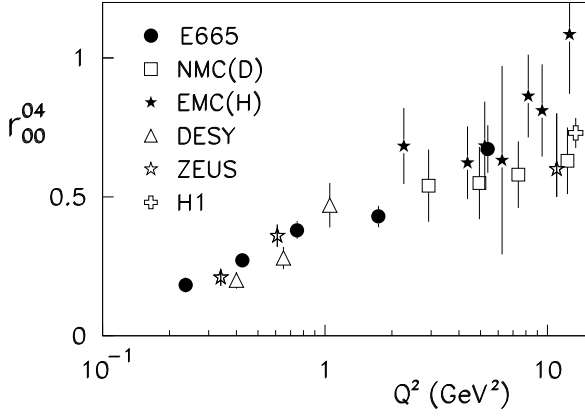**Fig. 39.** The spin density matrix element $Im(r_{1-1}^3)$ as a function of Q^2. Previous measurements from NMC [26] are shown for comparison. The errors on the E665 data points are statistical. The numerical values of the E665 data points are listed in Table 12.
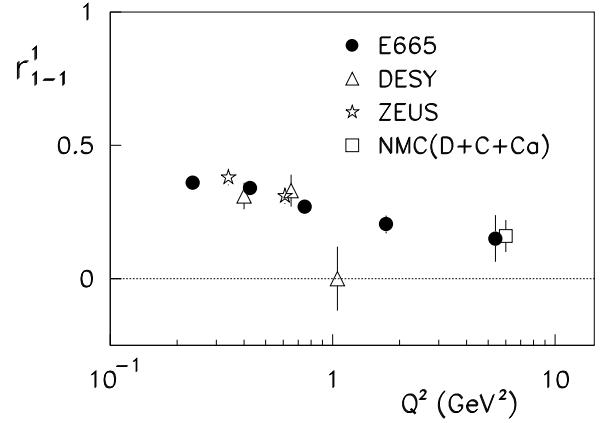
Fig. 40. The spin density matrix element r_{1-1}^1 as a function of Q^2. Previous measurements from DESY [12], NMC [26] and ZEUS [15] are shown for comparison. The errors on the E665 data points are statistical. The numerical values of the E665 data points are listed in Table 12.

ZEUS ($1332 < \nu < 4318$ GeV) experiments. A similar statement applies to r_{1-1}^{04} and r_{1-1}^1.

Further predictions in the case of SCHC are

$$r_{1-1}^{04} = r_{1-1}^3 = 0 \qquad (32)$$

and

$$R = \sigma_L/\sigma_T = \frac{1}{\epsilon} \cdot \frac{r_{00}^{04}}{1 - r_{00}^{04}} \;. \qquad (33)$$

If, in addition to SCHC, there is natural-parity exchange in the t-channel, r_{1-1}^1 and r_{00}^{04} are related by

$$r_{1-1}^1 = \frac{1}{2}(1 - r_{00}^{04}) \;. \qquad (34)$$

As can be seen from Figs. 38, 39 and Tables 12 and 13 the relations (32) and (34) are fulfilled within two standard deviations. The data are thus consistent with SCHC and t-channel natural-paritiy exchange.

Assuming SCHC, R has been determined using relation (33). The results are tabulated in Table 13 and plotted in Fig. 41. Similar to the case of r_{00}^{04}, R rises

strongly with increasing Q^2, reaching a value of 1 at $Q^2 \approx 2$ GeV^2.

A fit of the expression

$$R(Q^2) = C_0 (Q^2)^{C_1} \qquad (35)$$

to the E665 R values yields $C_0 = 0.66 \pm 0.05$ and $C_1 = 0.61 \pm 0.09$ with a χ^2/ndf of 0.98.

The measurements of R for diffractive ρ^0 productions can be used to determine a lower limit on $R^{inel} = \sigma_L^{inel}/\sigma_T^{inel}$ according to

$$R_{low}^{inel} = \frac{r}{(1-r)\epsilon + \frac{1}{R}} \;. \qquad (36)$$

Here $r = \sigma_{diff}(\rho^0)/\sigma_{inel}$ is the ratio of the cross section for diffractive ρ^0 production and the inelastic cross section. Assuming the measured R to be valid not only for single-diffraction but also for double-diffraction ρ^0 production, the r corresponding to the (SD+DD) ρ^0 cross section should be used in (36). The latter is obtained from r^{SD} by $r^{SD+DD} = r^{SD}/(1-h) = r^{SD}/0.8$. R_{low}^{inel}

Fig. 41. $R = \sigma_L/\sigma_T$ as determined from the measured values of r_{00}^{04} using (33), plotted as a function of Q^2. Previous measurements from DESY [12], EMC [23], NMC [26], ZEUS [15, 17, 18] and H1 [16] are shown for comparison. The errors on the E665 data points are statistical. The numerical values of the E665 data points are listed in Table 13.
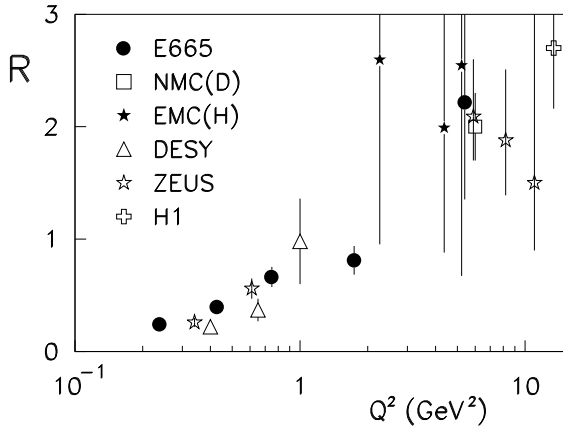
calculated in this way is listed in the last column of Table 13.

6 Summary

In this paper the diffractive production of ρ^0 in the reaction $\mu p \rightarrow \mu\rho^0 p$ has been studied in the kinematic region $20\,\mathrm{GeV} < \nu < 420\,\mathrm{GeV}$ and $0.15\,\mathrm{GeV}^2 < Q^2 < 20\,\mathrm{GeV}^2$. The present analysis confirms the results from previous experiments. Due to its higher statistical precision it provides more accurate measurements of the cross sections, the mass skewing parameter, the t' slope parameter and the spin density matrix elements. The results may be summarized as follows:

- The mass distribution of diffractively produced $\pi^+\pi^-$ systems in the ρ^0 mass region is skewed compared to a relativistic Breit-Wigner distribution, the skewness decreasing with increasing Q^2. (Figs. 17, 19).
- At the lowest Q^2 ($Q^2 \approx 0.15\,\mathrm{GeV}^2$) accessible in this experiment the cross section for the reaction $\mu p \rightarrow \mu\rho^0 p$ constitutes $\sim 8\%$ of the inelastic cross section. This fraction decreases strongly with increasing Q^2. At fixed Q^2, the fraction is consistent with being independent of x and ν (Figs. 20, 21 and 22).
- The main Q^2 dependence of the cross section $\sigma_{diff}(\gamma^* p \rightarrow \rho^0 p)$ for ρ^0 production by virtual photons is given by the ρ^0-propagator (Figs. 23 and 24).
- By extrapolating $\sigma(\gamma^* p \rightarrow \rho^0 p)$ to $Q^2 = 0$ a photoproduction cross section of $\sigma_0 = (10.30 \pm 0.33$ (stat.)) μb is obtained (Table 5). The contributions to the systematic error of σ_0 are $\pm 5\%$ from ratios of numbers of events, $\pm 13.7\%$ from kinematics dependent normalization uncertainties, and $\pm 1.8\%$ from the overall normalization uncertainty. σ_0 is reduced by 7.4% if the fraction of double-diffraction dissociation events amongst all diffractive events is assumed to be $h = 0.3$ instead of 0.2.

- In the region $t' < 0.5\,\mathrm{GeV}^2$, the t' distributions exhibit an exponential dependence, with a slope parameter $b = (7.0 \pm 0.2(\mathrm{stat.}) \pm 0.2(\mathrm{syst.}))\,\mathrm{GeV}^{-2}$. The slope parameter tends to decrease as Q^2 increases (Figs. 31, 32).
- The spin density matrix element r_{00}^{04} as determined from the distribution of the polar decay angle of the ρ^0 in the helicity frame rises rapidly in the Q^2 region of this experiment. Whereas the ρ^0 polarization is purely transverse at $Q^2 = 0$, the fraction of longitudinal ρ^0 is $\sim 50\%$ at $Q^2 \approx 2\,\mathrm{GeV}^2$ (Fig. 37).
- The values of the spin density matrix elements r_{00}^{04}, r_{1-1}^{04}, $Im\left(r_{1-1}^3\right)$ and r_{1-1}^1 are consistent with s-channel helicity conservation (SCHC) and natural-parity exchange in the t-channel (Tables 12 and 13).
- $R = \sigma_L/\sigma_T$ as determined from r_{00}^{04} assuming SCHC rises strongly with increasing Q^2 (Fig. 41).

References

1. J. Park et al., Nucl. Phys. B36 (1972) 404
2. R.M. Egloff et al., Phys. Rev. Lett 43 (1979) 657
3. D. Aston et al., Nucl. Phys. B209 (1982) 56
4. T.J. Chapin et al., Phys. Rev. D31 (1985) 17
5. M. Derrick et al. (ZEUS), Z. Phys. C63 (1994) 391
6. M. Derrick et al. (ZEUS), Z. Phys. C69 (1995) 39
7. S. Aïd et al. (H1), Nucl. Phys. B463 (1996) 3
8. M. Derrick et al. (ZEUS), DESY 96-183, Aug. 1996
9. ZEUS Collaboration, Ref. pa 02-050, Contribution to the XXVIII Conference on High Energy Physics, Warsaw, 1996
10. J.T. Dakin et al., Phys. Rev. D8 (1973) 687
11. J. Ballam et al., Phys. Rev. D10 (1974) 765
12. P. Joos et al., Nucl. Phys. B113 (1976) 53
13. D.G. Cassel et al., Phys. Rev. D24 (1981) 2787
14. I. Cohen et al., Phys. Rev. D25 (1982) 634
15. M. Derrick et al. (ZEUS), Phys. Lett. B356 (1995) 601
16. S. Aïd et al. (H1), Nucl. Phys. B468 (1996) 3
17. O. Lukina (ZEUS), Ref. pa 02-053, Contribution to the XXVIII Conference on High Energy Physics, Warsaw, 1996
18. J. Bulmahn (ZEUS), Ref. pa 02-028, Contribution to the XXVIII Conference on High Energy Physics, Warsaw, 1996
19. P.R. Newman et al. (H1), DESY 96-162, Aug. 1996
20. W.R. Francis et al., Phys. Rev. Lett. 38 (1977) 633
21. C. Del Papa et al., Phys. Rev. D19 (1979) 1303
22. W.D. Shambroom et al. (CHIO), Phys. Rev. D26 (1982) 1
23. J.J. Aubert et al. (EMC), Phys. Lett. 161B (1985) 203
24. J. Ashman et al. (EMC), Z. Phys. C39 (1988) 169
25. P. Amaudruz et al. (NMC), Z. Phys. C54 (1992) 239
26. M. Arneodo et al. (NMC), Nucl. Phys. B429 (1994) 503
27. M. Arneodo et al. (NMC), Il Nuovo Cim. 108A (1995) 1247
28. T.H. Bauer et al., Rev. Mod. Phys. 50 (1978) 261
29. A. Donnachie and P.V. Landshoff, Phys. Lett. B185 (1987) 403
30. I.F. Ginzburg et al., "Semihard quasi diffractive production of neutral mesons by off shell photons", to appear in Nucl. Phys. B
31. J. Nemchik et al. Phys. Lett. B341 (1994) 228
32. S.J. Brodsky et al., Phys. Rev. D50 (1994) 3134
33. L. Frankfurt et al., Phys. Rev. D54 (1996) 3194
34. J. Nemchik et al., DFTT71/95, KFA-IKP (TH)-24-95, hep-ph/9605231
35. A. Donnachie and P.V. Landshoff, Nucl. Phys. B311 (1989) 509
36. J.R. Cudell, Nucl. Phys. B336 (1990) 1
37. A. Donnachie and P.V. Landshoff, Phys. Lett. B348 (1995) 213
38. M.A. Pichowsky and T.-S.H. Lee, Phys. Lett. B379 (1996) 1
39. M.A. Pichowsky and T.-S.H. Lee, ANL-PHY-8529-TH-96,nucl-th/9612049
40. L.P.A. Haakman et al., NIKHEF 95-033, hep-ph/9507394
41. M.R. Adams et al., Nucl. Inst. and Meth. A291 (1990) 533
42. K. Goulianos, Phys. Rep. 101 (1983) 169
43. M.R. Adams et al., Phys. Rev. D54 (1996) 3006
44. A. Arvidson and B. Badelek, The GAMRAD program, NMC/92/5 (1992
45. L.W. Mo and Y.S. Tsai, Rev. Mod. Phys. 41 (1969) 205
46. Y.S. Tsai, SLAC-PUB-848 (1971)
47. R. Brun et al. GEANT: User guide and reference manual, CERN-DD/78/2 (1978)
48. A. Donnachie and P.V. Landshoff, Z. Phys. C61 (1994) 139
49. L.W. Whitlow et al., Phys. Lett. B250 (1990) 193
50. G. Ingelman, The Lund Monte Carlo for deep-inelastic lepton nucleon scattering (1983)
51. T. Sjöstrand, Comp. Phys. Comm. 39 (1986) 347
52. H. Fraas and D. Schildknecht, Nucl. Phys. B14 (1969) 543
53. N.N. Nikolaev et al., Z. Phys. A351 (1995) 435
54. H. Holtmann et al., Z. Phys. C69 (1996) 297
55. V. Del Duca at al., DESY 96-179, Aug. 1996
56. Y. Akimov et al., Phys. Rev. D14 (1976) 3148
57. L. Montanet et al., Phys. Rev. D50 (1994) 1177
58. L. van Hove, Phys. Lett. 28B (1969) 429
59. L. van Hove, Nucl. Phys. B9 (1969) 331
60. M. Deutschmann, Proc. of the Amsterdam Int. Conf on Elementary Particles, Eds. A.G. Tenner, M.J.G. Veltman (1972) 153
61. N.N. Nikolaev et al., Z. Phys. C53 (1992) 331
62. R.L. Cool et al., Phys. Rev. Lett. 48 (1982) 1451
63. M.R. Adams et al., Z. Phys. C71 (1996) 391
64. P. Söding, Phys. Lett. 19 (1966) 702
65. R. Ross and L. Stodolsky, Phys. Rev. 149 (1966) 1172
66. J. Pumplin, Phys. Rev. D2 (1970) 1859
67. G. Niesler et al., Phys. Lett. B389 (1996) 157
68. L.M. Barkov et al., Nucl. Phys. B256 (1985) 365
69. R. Spital and D.R. Yennie, Phys. Rev. D9 (1974) 126
70. L.N. Hand, Phys. Rev. 129 (1963) 1834
71. G.A. Schuler and T. Sjöstrand, Phys. Lett. B300 (1993) 169
72. G.A. Schuler and T. Sjöstrand, Nucl. Phys. B407 (1993) 539
73. B.Z. Kopeliovich et al., Phys. Lett. B309 (1993) 179
74. B.Z. Kopeliovich et al., Phys. Lett. B324 (1994) 469
75. M.R. Adams et al., Phys. Rev. Lett. 74 (1995) 1525
76. N.N. Nikolaev et al., Phys. Lett. B366 (1996) 337
77. K. Schilling and G. Wolf, Nucl. Phys. B61 (1973) 381
78. A.J. Malensek, private communication

Table 1. Definition of kinematic variables (see Fig. 1). The four-momenta, θ_μ, ν, z^h and p_{lab} are defined in the laboratory system. M_p is the proton mass.

Variable	Description
$k_\mu = (E_\mu, \mathbf{k}_\mu)$	4-momentum of the incident μ
$k'_\mu = (E'_\mu, \mathbf{k}'_\mu)$	4-momentum of the scattered μ
$P = (M_p, 0)$	4-momentum of the target proton
$q = (\nu, \mathbf{q}) = k_\mu - k'_\mu$	4-momentum of the virtual photon
$Q^2 = -q^2$	Negative square of 4-momentum transferred from the incident and the scattered μ
θ_μ	μ scattering angle
$W^2 = M_p^2 + 2M_p\nu - Q^2$	Total hadronic center of mass energy squared
$x = Q^2/2M_p\nu$	Bjorken scaling variable
$y = \nu/E_\mu$	Fractional leptonic energy transfer
M_X	Mass of a mesonic diffractive system X originating from the dissociation of the virtual photon
M_B	Mass of a baryonic diffractive system B originating from the dissociation of the proton
$k_X = (E_X, \mathbf{k}_X)$	4-momentum of the system X
$t = -(q - k_X)^2$	Negative square of 4-momentum transferred from the virtual photon and the system X
t_{min}	Minimum value of t for fixed ν, Q^2, M_X and M_B
$t' = t - t_{min}$	
$p = (E_{had}, \mathbf{p}_{had})$	4-momentum of a hadron
$z^h = E_{had}/\nu$	Fractional energy of a hadron
p_{lab}	Momentum of a hadron in the laboratory system
$p^h_\perp$	Transverse momentum of a hadron relative to the direction of the virtual photon in the cms
$x_F = p^*_L/(W/2)$	Feynman-x of a hadron (p^*_L is the longitudinal momentum of the hadron in the cms, relative to the direction of the virtual photon)
n_{ch}	Multiplicity of charged hadrons
$p_\perp$	Transverse momentum of a system of hadrons relative to the direction of the virtual photon in the cms
$z = \sum z^h$	Fraction of energy carried by a system of hadrons

Table 2. Number of events in the various samples of the experimental data.

sample	no. of events
inelastic	143502
extended diffractive	37567
diffractive	7717
extended diffractive ρ^0	14490
diffractive ρ^0	4943

Table 3. Results of fitting the expression (20) to the mass distribution in Fig. 16, excluding the ϕ mass region.

description of parameter	parameter	fitted value
fraction of ρ^0 events	a	$1.000^{+0.000}_{-0.006}$
central mass value of the ρ^0	M_ρ	(777 ± 2) MeV
width of the ρ^0	Γ_ρ	(146 ± 3) MeV
exponent in mass skewing factor	n	3.63 ± 0.09

Table 4. Fitted values of the mass skewing parameter n obtained by fitting expression (20) to the $\pi^+\pi^-$ mass distributions in different Q^2 regions. The parameters a and Γ_ρ were fixed at 1.0 and 146 MeV respectively and the fits were performed in the mass region $0.56 < M_X < 0.98$ GeV.

range in log (Q^2/GeV^2)	n	χ^2/ndf
all log Q^2	3.73 ± 0.27	1.16
0.82, −0.50	4.85 ± 0.42	1.46
−0.50, −0.25	3.80 ± 0.46	0.77
−0.25, 0.00	3.38 ± 0.58	0.72
0.00, 0.50	2.67 ± 0.60	1.03
0.50, 1.25	3.21 ± 2.31	0.96

Table 5. The cross section $\sigma_{diff}(\gamma^*p \to \rho^0 p) = \sigma_T + \epsilon\sigma_L$ as a function of Q^2, for all ν and for four regions of ν. The lower part of the table contains the results of fitting expressions (23) and (24) to the experimental data on $\sigma_{diff}(\gamma^*p \to \rho^0 p)$ in different bins of ν (Figs. 23 and 24). The cross sections, which are for single diffraction only, include a correction for the tails of the ρ^0 Breit-Wigner distribution. The errors given are statistical only. There are additional errors from the systematic error of r ($\pm 5\%$) and from the systematic error of F_2^p. The latter is composed of an overall normalization uncertainty of less than 1.8% and a kinematics dependent uncertainty, which is listed in the last column of Table 10. The effect on the results for the cross sections from a change of the fraction of double-diffraction dissociation events in the Monte Carlo simulation is discussed in Sect. 4.5. The Q^2 values were determined such that σ_{diff} at these Q^2 is equal to the tabulated σ_{diff}, assuming a Q^2 dependence of σ_{diff} according to (23) with $m = 2.51$ and $R(Q^2)$ from (35).

range in	Q^2	$\sigma(\gamma^*p \to \rho^0 p)$ (μb)				
$\log (Q^2/\text{GeV}^2)$	(GeV^2)	all ν	$20 < \nu < 90$ GeV	$90 < \nu < 150$ GeV	$150 < \nu < 250$ GeV	$250 < \nu < 420$ GeV
$-0.82, -0.75$	0.17	7.43 ± 1.03	4.75 ± 1.72	6.88 ± 1.83	6.99 ± 1.48	7.33 ± 1.66
$-0.75, -0.50$	0.25	5.03 ± 0.26	4.45 ± 0.35	4.54 ± 0.40	4.52 ± 0.38	5.96 ± 0.66
$-0.50, -0.25$	0.43	3.52 ± 0.16	2.79 ± 0.16	3.33 ± 0.24	3.89 ± 0.31	4.15 ± 0.47
$-0.25, -0.00$	0.76	1.84 ± 0.10	1.63 ± 0.11	2.19 ± 0.18	1.83 ± 0.17	2.01 ± 0.26
$0.00, 0.25$	1.35	0.875 ± 0.066	0.799 ± 0.079	0.846 ± 0.108	0.931 ± 0.112	0.913 ± 0.163
$0.25, 0.50$	2.39	0.315 ± 0.036	0.282 ± 0.051	0.331 ± 0.060	0.403 ± 0.073	0.283 ± 0.065
$0.50, 0.75$	4.23	0.126 ± 0.022	0.184 ± 0.043	0.152 ± 0.045	0.095 ± 0.029	0.125 ± 0.047
$0.75, 1.00$	7.51	0.048 ± 0.013	0.021 ± 0.013	0.026 ± 0.017	0.062 ± 0.023	0.063 ± 0.037
σ_0 (μb)		10.30 ± 0.33	8.81 ± 0.38	10.21 ± 0.52	10.13 ± 0.54	12.16 ± 0.89
ξ^2		-0.04 ± 0.02	-0.03 ± 0.02	-0.03 ± 0.02	-0.02 ± 0.03	-0.13 ± 0.05
χ^2/ndf		0.86	0.82	0.91	1.34	0.39

Table 6. The cross section $\sigma_{diff}(\gamma^*p \to \rho^0 p) = \sigma_T + \epsilon\sigma_L$ as a function of W, for four regions of Q^2. The cross sections, which are for single diffraction only, include a correction for the tails of the ρ^0 Breit-Wigner distribution. The errors given are statistical only. There are additional errors from the systematic error of r ($\pm 5\%$) and from the systematic error of F_2^p. The latter is composed of an overall normalization uncertainty of less than 1.8% and a kinematics dependent uncertainty, which is listed in the last column of Table 10. The effect on the results for the cross sections from a change of the fraction of double-diffraction dissociation events in the Monte Carlo simulation is discussed in Sect. 4.5. The Q^2 values were determined such that σ_{diff} at these Q^2 is equal to the tabulated σ_{diff}, assuming a Q^2 dependence of σ_{diff} according to (23) with $m = 2.51$ and $R(Q^2)$ from (35).

range in	$\langle W \rangle$	$\sigma(\gamma^*p \to \rho^0 p)$ (μb)			
ν (GeV)	(GeV)	$Q^2 = 0.24$ (GeV^2)	$Q^2 = 0.61$ (GeV^2)	$Q^2 = 1.84$ (GeV^2)	$Q^2 = 5.69$ (GeV^2)
20 - 90	10.1	4.57 ± 0.35	2.09 ± 0.09	0.485 ± 0.043	0.073 ± 0.017
90 - 150	14.9	4.73 ± 0.40	2.58 ± 0.15	0.511 ± 0.056	0.069 ± 0.019
150 - 250	19.3	4.78 ± 0.37	2.53 ± 0.16	0.592 ± 0.061	0.072 ± 0.017
250 - 420	24.1	6.07 ± 0.61	2.72 ± 0.24	0.497 ± 0.071	0.075 ± 0.025

Table 7. The cross sections σ_T, σ_L and $\sigma_T + \sigma_L$ for the reaction $\gamma^*p \to \rho^0 p$ as a function of Q^2. The cross sections, which are for single diffraction only, include a correction for the tails of the ρ^0 Breit-Wigner distribution. The errors given are statistical only. There are additional errors from the systematic error of r ($\pm 5\%$) and from the systematic error of F_2^p. The latter is composed of an overall normalization uncertainty of less than 1.8% and a kinematics dependent uncertainty, which is listed in the last column of Table 10. The effect on the results for the cross sections from a change of the fraction of double-diffraction dissociation events in the Monte Carlo simulation is discussed in Sect. 4.5. The Q^2 values were determined such that σ_{diff} at these Q^2 is equal to the tabulated σ_{diff}, assuming a Q^2 dependence of σ_{diff} according to (23) with $m = 2.51$ and $R(Q^2)$ from (35). $\langle \epsilon \rangle_1$ is the weighted average ($\int \epsilon\sigma_L \cdot d\nu dQ^2 / \int \sigma_L \cdot d\nu dQ^2$), where σ_L was parametrized according to (23) with $m = 2.51$ and $R(Q^2)$ from (35).

range in $\log (Q^2/\text{GeV}^2)$	Q^2 (GeV^2)	$\langle \epsilon \rangle_1$	$R(Q^2)$ using (35)	cross sections (in μb) for $\gamma^*p \to \rho^0 p$		
				σ_T	σ_L	$\sigma_T + \sigma_L$
$-0.82, -0.75$	0.17	0.76	0.22 ± 0.03	6.37 ± 0.89	1.39 ± 0.26	7.77 ± 1.08
$-0.75, -0.50$	0.25	0.80	0.28 ± 0.03	4.11 ± 0.23	1.15 ± 0.12	5.26 ± 0.28
$-0.50, -0.25$	0.43	0.81	0.39 ± 0.03	2.67 ± 0.13	1.051 ± 0.082	3.72 ± 0.17
$-0.25, 0.00$	0.76	0.81	0.56 ± 0.04	1.269 ± 0.073	0.708 ± 0.052	1.98 ± 0.10
$0.00, 0.25$	1.35	0.81	0.79 ± 0.08	0.533 ± 0.045	0.422 ± 0.040	0.955 ± 0.073
$0.25, 0.50$	2.39	0.81	1.12 ± 0.15	0.165 ± 0.022	0.185 ± 0.025	0.350 ± 0.040
$0.50, 0.75$	4.23	0.81	1.59 ± 0.29	0.055 ± 0.011	0.088 ± 0.017	0.143 ± 0.025
$0.75, 1.00$	7.51	0.81	2.26 ± 0.51	0.017 ± 0.005	0.038 ± 0.011	0.055 ± 0.015

Table 8. The cross section $(\sigma_T + \sigma_L)$ for the reaction $\gamma^* p \to \rho^0 p$ as a function of W, for four regions of Q^2. The cross sections, which are for single diffraction only, include a correction for the tails of the ρ^0 Breit-Wigner distribution. The errors given are statistical only. There are additional errors from the systematic error of r ($\pm 5\%$) and from the systematic error of F_2^p. The latter is composed of an overall normalization uncertainty of less than 1.8% and a kinematics dependent uncertainty, which is listed in the last column of Table 10. The effect on the results for the cross sections from a change of the fraction of double-diffraction dissociation events in the Monte Carlo simulation is discussed in Sect. 4.5. The Q^2 values were determined such that σ_{diff} at these Q^2 is equal to the tabulated σ_{diff}, assuming a Q^2 dependence of σ_{diff} according to (23) with $m = 2.51$ and $R(Q^2)$ from (35). $\langle \epsilon \rangle_1$ is the weighted average $\int \epsilon \sigma_L \cdot d\nu dQ^2 / \int \sigma_L \cdot d\nu dQ^2$, where σ_L was parametrized according to (23) with $m = 2.51$ and $R(Q^2)$ from (35).

range in ν (GeV)	$\langle W \rangle$ (GeV)	$\langle \epsilon \rangle_1$	$(\sigma_T + \sigma_L)$ (in μb) for $\gamma^* p \to \rho^0 p$
			$Q^2 = 0.24$ (GeV^2)	$Q^2 = 0.61$ (GeV^2)	$Q^2 = 1.84$ (GeV^2)	$Q^2 = 5.69$ (GeV^2)
20 - 90	10.1	0.99	4.58 ± 0.35	2.10 ± 0.09	0.487 ± 0.044	0.073 ± 0.017
90 - 150	14.9	0.95	4.78 ± 0.41	2.62 ± 0.15	0.523 ± 0.057	0.072 ± 0.020
150 - 250	19.3	0.84	4.94 ± 0.39	2.67 ± 0.17	0.641 ± 0.066	0.081 ± 0.019
250 - 420	24.1	0.59	6.64 ± 0.67	3.14 ± 0.28	0.620 ± 0.089	0.103 ± 0.034
			$(R = 0.27 \pm 0.03)$	$(R = 0.49 \pm 0.04)$	$(R = 0.96 \pm 0.11)$	$(R = 1.91 \pm 0.39)$

Table 9. The cross sections $\sigma_{diff}(\gamma^* p \to \rho^0 p) = \sigma_T + \epsilon \sigma_L$, σ_T and σ_L as a function of x, for four regions of Q^2. The cross sections, which are for single diffraction only, include a correction for the tails of the ρ^0 Breit-Wigner distribution. The errors given are statistical only. There are additional errors from the systematic error of r ($\pm 5\%$) and from the systematic error of F_2^p. The latter is composed of an overall normalization uncertainty of less than 1.8% and a kinematics dependent uncertainty, which is listed in the last column of Table 10. The effect on the results for the cross sections from a change of the fraction of double-diffraction dissociation events in the Monte Carlo simulation is discussed in Sect. 4.5.

range in $\log(x)$	$\sigma_{diff} = \sigma_T + \epsilon \sigma_L$ for $\gamma^* p \to \rho^0 p$ (μb)
	range in $\log(Q^2/\text{GeV}^2)$:
	$(-0.82, -0.5)$	$(-0.5, 0.0)$	$(0.0, 0.5)$	$(0.5, 1.0)$
$-3.67, -3.33$	6.69 ± 0.71			
$-3.33, -3.00$	5.02 ± 0.36	4.10 ± 0.41		
$-3.00, -2.67$	4.55 ± 0.37	2.53 ± 0.16	0.972 ± 0.280	
$-2.67, -2.33$	3.77 ± 0.42	2.09 ± 0.12	0.630 ± 0.070	
$-2.33, -2.00$	7.48 ± 1.76	1.86 ± 0.12	0.474 ± 0.051	0.114 ± 0.036
$-2.00, -1.67$		1.42 ± 0.19	0.384 ± 0.049	0.098 ± 0.022
$-1.67, -1.33$			0.377 ± 0.081	0.041 ± 0.011
$-1.33, -1.00$				0.040 ± 0.018

range in $\log(x)$	σ_T for $\gamma^* p \to \rho^0 p$ (μb)
	range in $\log(Q^2/\text{GeV}^2)$:
	$(-0.82, -0.5)$	$(-0.5, 0.0)$	$(0.0, 0.5)$	$(0.5, 1.0)$
$-3.67, -3.33$	5.85 ± 0.63			
$-3.33, -3.00$	4.09 ± 0.31	3.34 ± 0.33		
$-3.00, -2.67$	3.57 ± 0.30	1.88 ± 0.12	0.703 ± 0.203	
$-2.67, -2.33$	2.93 ± 0.33	1.42 ± 0.09	0.402 ± 0.047	
$-2.33, -2.00$	5.73 ± 1.36	1.22 ± 0.08	0.259 ± 0.031	0.059 ± 0.019
$-2.00, -1.67$		0.90 ± 0.13	0.197 ± 0.027	0.041 ± 0.010
$-1.67, -1.33$			0.181 ± 0.041	0.014 ± 0.004
$-1.33, -1.00$				0.013 ± 0.006

range in $\log(x)$	σ_L for $\gamma^* p \to \rho^0 p$ (μb)
	range in $\log(Q^2/\text{GeV}^2)$:
	$(-0.82, -0.5)$	$(-0.5, 0.0)$	$(0.0, 0.5)$	$(0.5, 1.0)$
$-3.67, -3.33$	1.40 ± 0.22			
$-3.33, -3.00$	1.14 ± 0.13	1.25 ± 0.15		
$-3.00, -2.67$	1.02 ± 0.12	0.86 ± 0.07	0.494 ± 0.145	
$-2.67, -2.33$	0.85 ± 0.12	0.71 ± 0.05	0.326 ± 0.041	
$-2.33, -2.00$	1.75 ± 0.44	0.64 ± 0.05	0.246 ± 0.031	0.088 ± 0.029
$-2.00, -1.67$		0.53 ± 0.08	0.191 ± 0.027	0.072 ± 0.017
$-1.67, -1.33$			0.197 ± 0.044	0.027 ± 0.008
$-1.33, -1.00$				0.027 ± 0.013

Table 10. Average values of Q^2, ν, W, x and ϵ for the different bins in $\log(Q^2/\mathrm{GeV}^2)$ or ν. The average of a quantity v was determined as $\langle v \rangle = \int v\sigma_{diff} \cdot d\nu dQ^2 / \int \sigma_{diff} \cdot d\nu dQ^2$, where σ_{diff} was parametrized according to (23) with $m = 2.51$ and $R(Q^2)$ from (35). The last but one column contains the number of events in the diffractive ρ^0 sample for the respective Q^2 or ν interval. The relative systematic error of F_2^p due to kinematics dependent uncertainties is listed in the last column. These errors were calculated from the errors given in [43], averaging over the respective kinematic range.

range in $\log(Q^2/\mathrm{GeV}^2)$	$\langle Q^2 \rangle$ (GeV^2)	$\langle \nu \rangle$ (GeV)	$\langle W \rangle$ (GeV)	$\langle x \rangle$	$\langle \epsilon \rangle$	no. of ρ^0 events	$\Delta F_2^p / F_2^p$ (syst.) (%)
−0.82, −0.75	0.16	224	20.0	0.0005	0.764	130	
−0.75, −0.50	0.24	197	18.5	0.0010	0.809	1020	19.3
−0.50, −0.25	0.43	190	18.1	0.0019	0.819	1544	6.3
−0.25, 0.00	0.76	189	18.0	0.0034	0.822	1221	5.1
0.00, 0.25	1.33	187	17.9	0.0060	0.824	599	3.5
0.25, 0.50	2.36	185	17.8	0.0108	0.828	250	3.4
0.50, 0.75	4.18	184	17.7	0.0192	0.831	124	3.3
0.75, 1.00	7.41	182	17.5	0.0345	0.834	44	3.2
1.00, 1.25	13.2	180	17.2	0.0617	0.836	11	3.6
−0.82, −0.50	0.23	201	18.7	0.0010	0.802	1150	19.3
−0.50, 0.00	0.59	189	18.1	0.0026	0.820	2765	5.7
0.00, 0.50	1.76	186	17.9	0.0080	0.826	849	3.5
0.50, 1.00	5.39	183	17.6	0.0249	0.832	168	3.3
−0.82, 1.00	1.40	190	18.1	0.0064	0.819	4932	13.7
range in ν (GeV)							
20 - 90	1.48	56	10.1	0.0162	0.990	2018	26.2
90 - 150	1.44	120	14.9	0.0065	0.952	1170	15.0
150 - 250	1.39	199	19.3	0.0038	0.845	1115	5.0
250 - 420	1.31	311	24.1	0.0023	0.598	629	7.4

Table 11. Results of fits of the expression $d\sigma/dt' = Ae^{-bt'}$ to the experimental t' distributions and of the expression $d\sigma/dp_\perp^2 = Ce^{-d \cdot p_\perp^2}$ to the experimental $p_\perp^2$ distributions. The values in the columns labelled as SD and SD + DD are obtained from the distributions, which exclude or include the full contribution from double-diffraction dissociation. The χ^2 per degree of freedom is given in brackets.

range in $\log(Q^2/\mathrm{GeV}^2)$	t' range (GeV^2)	SD b (GeV^{-2})		SD + DD b (GeV^{-2})		$p_\perp^2$ range (GeV^2)	SD d (GeV^{-2})		SD + DD d (GeV^{-2})	
−0.82, −0.50	0.0 - 0.5	8.3 ± 0.4	(2.2)	7.5 ± 0.4	(2.6)	0.0 - 0.5	8.1 ± 0.5	(2.1)	7.7 ± 0.4	(2.5)
−0.50, −0.25	0.0 - 0.5	7.7 ± 0.4	(1.1)	6.9 ± 0.3	(1.2)	0.0 - 0.5	7.8 ± 0.4	(1.0)	7.3 ± 0.3	(1.7)
−0.25, 0.00	0.0 - 0.5	6.5 ± 0.4	(2.7)	5.9 ± 0.4	(2.5)	0.0 - 0.5	6.6 ±0.4	(2.7)	6.0 ± 0.3	(2.1)
0.00, 0.50	0.0 - 0.5	6.7 ± 0.5	(0.5)	5.8 ±0.4	(0.6)	0.0 - 0.5	6.2 ± 0.5	(0.7)	6.4 ± 0.4	(0.8)
0.50, 1.25	0.0 - 0.5	6.0 ± 1.3	(0.9)	5.9 ± 1.2	(0.9)	0.0 - 0.5	6.9 ± 1.7	(1.0)	6.8 ± 1.6	(1.0)
all $\log(Q^2/\mathrm{GeV}^2)$	0.0 - 0.5	7.0 ± 0.2	(3.8)	6.3 ± 0.2	(4.3)	0.0 - 0.5	7.1 ± 0.2	(3.7)	6.7 ± 0.2	(4.7)
all $\log(Q^2/\mathrm{GeV}^2)$	0.05 - 0.5	6.4 ± 0.2	(2.1)	5.8 ± 0.2	(2.2)	0.05 - 0.5	6.6 ± 0.3	(2.8)	6.2 ± 0.2	(3.3)
all $\log(Q^2/\mathrm{GeV}^2)$	0.0 - 1.0	6.5 ± 0.2	(3.3)	5.8 ± 0.1	(4.2)	0.0 - 1.0	6.7 ± 0.2	(2.5)	6.2 ± 0.2	(3.8)

Table 12. Spin density matrix elements as determined from fits of the expressions (29), (30), and (31) to the experimental distributions. $\langle \epsilon \rangle_2$ is the weighted average $(\int \epsilon \Gamma_T \sigma_L \cdot d\nu dQ^2 / \int \Gamma_T \sigma_L \cdot d\nu dQ^2)$, where σ_L was parametrized according to (23) with $m = 2.51$ and $R(Q^2)$ from (35).

range in $\log(Q^2/\mathrm{GeV}^2)$	$\langle \epsilon \rangle_2$	r_{00}^{04}	r_{1-1}^1	r_{1-1}^{04}	$Im(r_{1-1}^3)$
−0.82, −0.50	0.91	0.182 ± 0.027	0.360 ± 0.023	−0.001 ± 0.027	0.002 ± 0.096
−0.50, −0.25	0.93	0.271 ± 0.025	0.340 ± 0.021	−0.024 ± 0.024	0.003 ± 0.092
−0.25, 0.00	0.93	0.381 ± 0.032	0.270 ± 0.026	−0.030 ± 0.026	0.003 ± 0.108
0.00, 0.50	0.93	0.429 ± 0.039	0.203 ± 0.033	−0.028 ± 0.034	−0.141 ± 0.130
0.50, 1.00	0.93	0.672 ± 0.086	0.151 ± 0.087	0.055 ± 0.071	0.339 ± 0.312

Table 13. Results obtained assuming s-channel helicity conservation. The column labelled with r^1_{1-1} (SCHC) contains r^1_{1-1} as determined from r^{04}_{00} using (34). The ratio $R = \sigma_L/\sigma_T$ of cross sections for the production of ρ^0 mesons by longitudinally and transversely polarized virtual photons was determined from the measurements of r^{04}_{00} using (33). The lower limits on $R^{inel} = \sigma^{inel}_L/\sigma^{inel}_T$ as calculated from R and r^{SD+DD} using (36) are listed in the last column.

range in $\log (Q^2/\text{GeV}^2)$	r^1_{1-1} (SCHC)	$R = \sigma_L/\sigma_T$	R^{inel}_{low}
$-0.82,\ -0.50$	0.409 ± 0.014	0.245 ± 0.044	0.018 ± 0.003
$-0.50,\ -0.25$	0.364 ± 0.013	0.401 ± 0.052	0.023 ± 0.002
$-0.25,\ \ \ 0.00$	0.310 ± 0.016	0.664 ± 0.090	0.025 ± 0.002
$\ \ \ 0.00,\ \ \ 0.50$	0.285 ± 0.019	0.811 ± 0.128	0.016 ± 0.002
$\ \ \ 0.50,\ \ \ 1.00$	0.164 ± 0.043	2.216 ± 0.863	0.010 ± 0.002